

## Distribution Agreement

In presenting this thesis or dissertation as a partial fulfillment of the requirements for an advanced degree from Emory University, I hereby grant to Emory University and its agents the non-exclusive license to archive, make accessible, and display my thesis or dissertation in whole or in part in all forms of media, now or hereafter known, including display on the world wide web. I understand that I may select some access restrictions as part of the online submission of this thesis or dissertation. I retain all ownership rights to the copyright of the thesis or dissertation. I also retain the right to use in future works (such as articles or books) all or part of this thesis or dissertation.

Signature:

---

Grant Williams

---

Date

Image Processing for the Structural Analysis of Respiratory Syncytial Virus by Cryo-  
Electron Tomography

By

Grant Martin Williams  
Masters of Science

Graduate Division of Biological and Biomedical Science  
Microbiology and Molecular Genetics

---

Elizabeth R. Wright, Ph.D.  
Advisor

---

Graeme L. Conn, Ph.D.  
Committee Member

---

Arash Grakoui, Ph.D.  
Committee Member

---

James Nagy, Ph.D.  
Committee Member

---

Raymond Schinazi, Ph.D.  
Committee Member

Accepted:

---

Lisa A. Tedesco, Ph.D.  
Dean of the James T. Laney School of Graduate Studies

---

Date

Image Processing for the Structural Analysis of Respiratory Syncytial Virus by Cryo-  
Electron Microscopy

By

Grant Martin Williams

B.S., Georgia Institute of Technology, 2005

Advisor: Elizabeth R. Wright, Doctor of Philosophy

An abstract of

A thesis submitted to the Faculty of the

James T. Laney School of Graduate Studies of Emory University

in partial fulfillment of the requirements for the degree of

Master of Science

in

Graduate Division of Biological and Biomedical Science

Microbiology and Molecular Genetics

2012

## Abstract

### Image Processing for the Structural Analysis of Respiratory Syncytial Virus by Cryo-Electron Tomography

By Grant Martin Williams

Respiratory Syncytial Virus (RSV) is a member of the Paramyxoviridae family of viruses. RSV contains a single-stranded, negative sense RNA genome, which is encapsidated by the viral nucleocapsid, phosphoprotein, and RNA-dependent RNA polymerase. The four macromolecules combined form the helical ribonucleoprotein (RNP) complex. It is the RNP that must be transferred from an infected cell to a new cell in order for the infection process to continue.

In this study, cryo-electron tomography (cryo-ET) was used to characterize the three-dimensional (3D) structure of purified RSV virions. The RNP was resolved as hollow tubes with helical spokes of an approximately 9nm width in X-Y cross-sections. A module, TubeTracker, was developed for the Amira software programs in order to objectively map the trajectory of RNP through the 3D volumes of the RSV virions. Several denoising algorithms were generated to improve the signal to noise ratio of the 3D data to increase the likelihood of accurate feature tracking.

Model toroids representing hollow tubular trajectories were first developed to assess the functionality of TubeTracker under each of its programmed conditions. The model toroids were tracked successfully under both the ideal noise-free situation as well as with the addition of increasing amounts of white, speckle noise to the model toroid volumes. During the application of TubeTracker to the RSV tomograms, the program performed for several iterations, then trajectory tracking was prone to error. The failure of the TubeTracker to function with the cryo-ET data of RSV was possibly due to poor feature cross-correlation due to missing-wedge effects, angular search range and increments, or limited voxel intensity ranges.

Image Processing for the Structural Analysis of Respiratory Syncytial Virus by Cryo-  
Electron Tomography

By

Grant Martin Williams

B.S., Georgia Institute of Technology, 2005

Advisor: Elizabeth Wright, Doctor of Philosophy

A thesis submitted to the Faculty of the  
James T. Laney School of Graduate Studies of Emory University  
in partial fulfillment of the requirements for the degree of  
Master of Science  
in  
Graduate Division of Biological and Biomedical Science  
Microbiology and Molecular Genetics

2012

## ACKNOWLEDGEMENTS

First and foremost, I would like to thank my advisor, Dr. Elizabeth R. Wright, for allowing me to realize my passion in computer programming in combination with biological technology and providing guidance, resources, and mentorship throughout these years to accomplish my goals. I thank my committee members for their support both in the initial stages of my graduate work and the later stages as my project became more defined and intensive. Special thanks to Dr. James Nagy for his support and helpful conversations in the operations of the programs designed and presented in this thesis and for aid in finding and understanding literature relevant to these ends. I also thank the members of the Wright lab, Drs. Ricardo Guerrero-Ferreira, Jens Holl, and Gabriella Kiss, for their advice and assistance in laboratory procedures, manuscript preparation, and general support on a daily basis. Finally, I would like to thank my father, Bill Williams, for instilling in me a drive to succeed and do great things, and my husband, Shane Desmond-Williams, for his daily support, ideas, and consoling in hard times, especially during my recovery following my traumatic brain injury in 2011.

**TABLE OF CONTENTS**

Distribution Agreement	i
Approval Form	ii
Abstract Cover Page	iii
Abstract	iv
Thesis Cover Page	v
Acknowledgements	vi
List of Figures	viii
List of Abbreviations	ix
List of Tables	x
CHAPTER I – INTRODUCTION	1
CHAPTER II – MATERIALS AND METHODS	14
CHAPTER III – RESULTS	18
CHAPTER IV – DISCUSSION	40
REFERENCES	45

## LIST OF FIGURES

		Page
1. Fig. 1:	Three groups of RSV particles classified by structural densities present in 2D cross-sections of tomograms	19
2. Fig. 2:	Linear profile of electron densities through the RSV membrane	21
3. Fig. 3A:	Search sphere for generation of tangent planes	23
4. Fig. 3B:	Center coordinates for tangent plane generation along normal vectors to search sphere	23
5. Fig. 3C:	Tangent plane creation at center points on search sphere	24
6. Fig. 3D:	Creation of search sphere at center coordinate of tangent plane with best cross-correlation value	24
7. Fig. 4A:	Planar toroid volume used for testing of TubeTracker module	26
8. Fig. 4B:	LineSet object showing trajectory from TubeTracker for 50 iterations through transparent surfaces of 4A	27
9. Fig. 4C:	Tangent planes of first iteration of TubeTracker usage with planar toroid	27
10. Fig. 5:	Generation of tangent volume as series of tangent planes	28
11. Fig. 6A:	Surface renderings of tubular helix	30
12. Fig. 6B:	LineSet object showing trajectory from TubeTracker performance of 50 iterations through transparent surfaces of tubular helix of 6A	30
13. Fig. 7A:	TubeTracker performance of 100 iterations on tubular helix of Fig. 6 with one addition of white noise	31
14. Fig. 7B:	TubeTracker performance of 100 iterations on tubular helix of Fig. 6 with two additions of white noise	32
15. Fig. 8A:	3x3 Mean filter vs. 3x3 Selective Mean filter	34
16. Fig. 8B:	3x3 Median filter vs. 3x3 Selective Median filter	36
17. Fig. 8C:	3x3 Bilateral filter	38
18. Fig. 8D:	SNR measurements for five iterations of mean, median, and bilateral filters	39



**LIST OF ABBREVIATIONS**

1D – One-dimensional

2D – Two-dimensional

3D – Three-dimensional

Cryo-EM – Cryo-Electron Microscopy

Cryo-ET – Cryo-Electron Tomography

DFT – Discrete Fourier Transform

EM – Electron Microscopy

ET – Electron Tomography

F – Fusion protein

FT – Fourier Transform

FFT – Fast Fourier Transform

G – Attachment protein

IDFT – Inverse Discrete Fourier Transform

M – Matrix protein

N – Nucleocapsid protein

OsO<sub>4</sub> – Osmium tetroxide

P – Phosphoprotein

RNP – Ribonucleoprotein complex

RSV – Respiratory Syncytial Virus

SEM – Scanning Electron Microscopy

SNR – Signal-to-Noise Ratio

TEM – Transmission Electron Microscopy

VLP – Virus-like particle

**LIST OF TABLES**

	Page
Table 1: Image data types and value ranges	6

## CHAPTER 1

### INTRODUCTION

#### ELECTRON MICROSCOPY

##### History

Microscopy's origins date back to 1665, when Robert Hooke published his observations of cells in a slice of cork with a lens that magnified object 30 times their original size. Eleven years later in 1676, using a lens of his own making, Antoni van Leeuwenhoek published his observations of "small living animals" in material taken from his teeth [1]. Lenses for visualization of biological structures at sub-millimeter scale continued to progress for light microscopy for the next 250 years, allowing distinction of structures separated by  $0.2\mu\text{m}$ . In 1924, de Broglie's publication indicated that electrons, like all matter, exhibited wave-like characteristics. This physical attribute provided the potential for electrons to be used for visualization of structures at resolutions 1,000-fold greater than that of visible light. In 1931, Ernst Ruska and Max Knoll developed the transmission electron microscope, capable of magnification superior to confocal imaging due to the shorter wavelength of the electrons transmitted through the specimen [2].

After this breakthrough in imaging was engineered, improvements to the microscope hardware and biological sample preservation further increased the achievable resolution of the electron microscope. Obtaining adequate specimen fixation for transmission electron microscopy (TEM) was the first hurdle to overcome, as samples are prone to damage upon exposure to the electron beam, resulting in alterations to nanometer-scale structures which detracts from the native conformations of the macromolecules within. For this purpose, osmium tetroxide ( $\text{OsO}_4$ ) was tested and found to provide adequate fixation of biological samples without interfering side reactions known to happen with formaldehyde-based reagents [3]. Later, potassium

permanganate was used as a fixative and demonstrated usefulness as a stain to enhance contrast despite the lighter atomic weight of manganese as compared to osmium [4]. One drawback of permanganate fixation, however, was that it abolished enzymatic activity of the fixed proteins, while  $\text{OsO}_4$  only fixed lipid membranes through a reaction with fatty acid side chains. In light of this, glutaraldehyde was later determined to be an adequate preliminary fixative to cross-link protein moieties while leaving their activity unchanged before following with  $\text{OsO}_4$  to stabilize membranes and provide heavy metal contrast [5].

These fixation and staining methods allow greater contrast between biological electron densities compared to an aqueous supernatant or cytoplasmic milieu, but the price of this enhanced contrast is a loss of native-state conformation of the macromolecules within the sample being imaged. As initial fixation procedures have been shown to vary the behavior of biological specimens when viewed by TEM [6], rapid freezing of samples was utilized instead to circumvent these structural alterations while immobilizing the material of interest in vitreous ice. Cryo-preservation methods have been used since for sectioning of thick specimens by ultramicrotomy [7-12]. When this procedure was used with prokaryotic organisms, it was shown to circumvent the creation of mesosomes, which were concluded to be artifacts of the fixation and staining procedure [12]. For thin specimens, preservation involves plunge-freezing into a liquid cryogen that instantly drops the temperature within the sample below water's glass temperature,  $T_g$ , such that this aqueous volume will be immobilized in a vitreous form without becoming crystalline ice, which distorts microscopic structures by expansion during the freezing process [13, 14].

### **Biological image analysis from EM**

To extract more than simple two-dimensional (2D) information from EM images, computational analysis was devised by extrapolating from procedures already known in X-ray crystallography. The Fourier transform (FT) began as a mathematical concept developed by Jean Baptiste Joseph Fourier to prove that any function, even piece-wise discontinuous functions but especially repetitive continuous functions, could be represented by a simple sum of sines and cosines weighted by different frequencies [15]. Calculating the discrete FT (DFT) of a one-dimensional (1D) signal of real values results in a complex series of values that can be represented as magnitudes, or power spectra, and phases around a unit circle. When applied to a 2D image, the magnitude and phase present themselves as a diffraction pattern, with pixel values representing the magnitude and their location relative to the center by the phase. The phase problem, as encountered with crystallography, is that the diffraction pattern of an experiment gives only the magnitude, leaving the phase to be approximated by various methods such as heavy atom replacement or iterative computational solutions [16, 17]. With EM, though, the DFT of a real-valued image produces both the magnitude and phase such that the inverse transform (IDFT) can reproduce the original image exactly.

The computational complexity of the calculation of the DFT was once  $O(N^2)$  until the development of a Fast Fourier Transform (FFT) algorithm that reduced its complexity to  $O(N \log_2 N)$  [18]. By reorganizing an input array of values with a length equal to a power of two, each of the  $N$  values are summed and multiplied by the corresponding trigonometric values in  $\log_2 N$  stages instead of  $N$ . This improvement allowed images collected through EM to be processed more quickly and accurately.

Now that researchers had greater ease of conversion from traditional Real-only space (i.e. Real pixel values with Imaginary components set to zero) to the complex plane, they were able to extrapolate frequency information from the FFT of TEM

projections. In 1968, De Rosier and Klug used the Fourier transform of the T4 bacteriophage tail to decipher its outer helical sheath as a distinct entity from the inner protein core used for transmission of DNA to the host *E. coli* cell. By filtration of the phage tail projection according to the optical diffraction pattern (i.e. the FFT of the image with quadrant swapping applied), they were able to construct the reverse FFT, revealing an image in which two helices were present at different depths within the tail. From this Fourier analysis, they concluded that since a 2D projection of a helical structure represents projections from various angles equally, a 3D model may be constructed by treating the rows of the image as a series of 1D projections, each viewed from a different angle. The following reconstruction would involve aligning each projection's 1D FFT into a radial 2D array and calculating the reverse transform of the aligned 2D Fourier amplitudes and phases to reform the cross-section of the original 3D helix [19], known today as helical reconstruction.

This key piece of research brought together the experience of crystallography with the imaging capabilities of the electron microscope through Fourier analysis. In implementing the Fourier projection theorem, they successfully showed that a single, 2D projection of a helix could result in complete reconstruction of the 3D helix itself by treating each row of the image as a series of 1D projections along a series of viewing angles because the full helix volume could be represented in Fourier space. It was then postulated that structures lacking helical symmetry can be reconstructed by the same computational framework, but the projections themselves must be derived by physically tilting the specimen in the microscope to collect the 2D images. In a follow-up article, R.A. Crowther, laid out an interpolation mechanism by which a series of 2D projection images could be transformed to Fourier space, row by row, then the series of 1D complex values, weighted by either a least-squares method or cylindrical expansion, were converted to a 2D matrix that could be subjected to the reverse Fourier transform

to obtain Real pixel values for each slice of a row in a 3D volume [20]. This method of 3D reconstruction is more commonly known today as “R-weighted back-projection”, as the bilinear interpolation mechanism [21] weights complex values of the Fourier transform in favor of projections collected closest to zero degrees of tilt. Years later, these ideas were implemented into the IMOD program [22] for a user-friendly way of combining EM tilt series images into a 3D image reconstruction currently used by laboratories around the world for electron tomography (ET).

Additionally, this research proposed that manual tilting need not be applied if projections of single structures could be captured at various viewing angles in a single image. The work with T4 bacteriophage took advantage of the repetitive symmetry of the helix in the structure of the specimen, but if an object had no symmetry and several samples were present in a single image, then the application of tomographic reconstruction could be applied to individual images of each particle as if they were part of a tilted series of projections. The challenge with this analysis is to accurately estimate the differences in viewing axis relative to a common direction. To combat this challenge, programs were developed for a systematic way of classifying individual particles into groups of relatedness then arranging them as Crowther did in Fourier space according to their estimated projection viewing angle [23-26] resulting in the advent of single-particle analysis. By using this method to more completely fill the complex plane with values instead of bilinear interpolation, enhanced resolution could be obtained by having more individual projections to work with in a single image than could be obtained by imaging a single structure over a series of tilt angles through tomography and does not suffer the missing wedge effect resulting from incomplete filling of densities in Fourier space along the missing projection axes [27].

## **Image Capture and Processing**

While the interactions between an electron and a sample of interest could be qualified by formation of an image on a film, there remained a gap in the level of detail that could be extrapolated from this information. After the creation of computers and image scanners, however, images collected through EM could be converted to digital information represented by pixels in a 2D array each with a distinct value according to the sampling of the conversion process. This milestone in image analysis allowed the field of digital image processing to come to the world of EM, since our perception of grayscale intensity could now be quantified in a numerical fashion. Further advancement came with the advent of charge-coupled device (CCD) cameras capable of converting transmitted electrons to electronic signals that are interpreted by a computer into an image [28]. As image data from EM is derived from an electron source of wavelength outside the visible spectrum, only grayscale images may be obtained from the microscope's CCD; therefore, all pixel values derived from the transmission of electrons in EM experiments can be limited to a set range of integer values based on the bit level of the data type chosen by the user (Table 1).

**Table 1: Image data types and value ranges**

<b>Data Type</b>	<b>Minimum</b>	<b>Maximum</b>
8-bit ("byte")	0	255
signed 16-bit ("short")	-32768	32767
unsigned 16-bit ("ushort")	0	65535

Grayscale images and volumes may simply be classified as a 2- or 3D array of integer values, but qualification by the eye is what allows us to determine the importance of this digital information. Because of this, we are able to visually determine which



groups of grey values constitute valid structural information (i.e. signal) and which values correspond to other, unimportant substances (i.e. noise). Objective classification of a pixel as signal or noise in an image can be estimated statistically by a computer, but the definitive distinction tends to require user intervention to correct for significant noise interference in structural signals. The ratio of mean to standard deviation ( $\sigma$ ) among pixels in a user-defined neighborhood is one way to quantitatively measure the contribution of noise to an image in a local analysis [29]. Efforts are still underway to define the most effective method for completely removing noise from an image while leaving the structural signal untouched.

In terms of structural analysis, sample averaging tends to be the most effective way to retain information derived from signal while simultaneously removing the influence of unwanted noise. To average like signal components, however, it is necessary to overcome the interference of noise to the alignment, or registration, of true signal for accurate computation. It is logical, then, that operations to remove potential noise (i.e. denoise) from image data must be applied so that alignment and classification of like structures can be more accurately attained. The measurements and analyses would then be applied to the raw, unprocessed data so that intensity values indicative of signal would be averaged together while the highly variable values associated with noise will be averaged away, resulting in a reconstruction with potentially greater quality than could be obtained with no user intervention [30]. This idea is supported by the nature of common alignment strategies using cross-correlation, or the Pearson correlation coefficient:

$$P = \frac{1}{\sigma_1 \sigma_2 (WH - 1)} \sum_{y=0}^{H-1} \sum_{x=0}^{W-1} [I_1(x, y) - \mu_1][I_2(x, y) - \mu_2]$$

where  $\sigma_1$  and  $\sigma_2$  are the standard deviations of image 1 ( $I_1$ ) and image 2 ( $I_2$ ), respectively, and  $\mu_1$  and  $\mu_2$  are the mean values of  $I_1$  and  $I_2$ .

The image to align is typically cropped to the width (W) and height (H) of the object of interest and is then cross-correlated to the reference image at offsets that cover the full area of the reference. The resulting value, P, will range between -1 and +1, indicating a poor alignment at -1 and a perfect alignment at +1. If a positive value does not calculate to exactly 1, then the highest value calculated represents the lateral and longitudinal offsets required to best align the images. As each image is collected separately at different times,  $\sigma_1$  and  $\sigma_2$  will differ even if they represent the same specimen at the same location. By reducing the difference between a pixel's value and the image mean, the standard deviation will be reduced, thereby limiting the contribution of noise values to the alignment calculation. This alignment procedure is used in the tomographic reconstruction program IMOD to ensure uniform axial alignment of each tilt series image before back-projection.

The origins of noise in EM vary based on the collection methods chosen by the researcher and the contents of the sample to be imaged. At the onset of EM, image data was retrieved by interaction of the transmitted electron beam with a film that, after the advent of the computer, would be scanned to digital information, potentially subject to errors in sampling distance. As collection means advanced to CCD cameras, an additional contribution of noise came from the conversion of measurements of electron detection via a phosphor coated screen to integer quantification in a digital image. The preparation method, too, can be subject to noise during the collection of images from the microscope. As frozen samples are subject to irradiation from the electron beam, the total dose must be minimized such that the specimen is not degraded during the collection procedure [31]. This reduction in transmitted electrons per square Angstrom results in increased shot noise per image collected of an individual sample [32].

Shot noise can be modeled as white, representing a Gaussian distribution, but its treatment method can vary from local filters, which operate on a small window of user-

defined dimensions, to global filters, which alter the image as a whole instead of smaller windows within it [15]. Several local filters have been developed and applied through the years, such as the mean, median, min, max, midpoint, Gaussian [15, 33], and bilateral filters [34], while some global applications have proven successful in contrast adjustment and shot noise removal, such as histogram manipulation [35], non-linear anisotropic diffusion [36], gamma transformations, and intensity thresholding [15]. The drawback of both local and global operations in their raw form is that they apply a user-defined mechanism for noise reduction without regard to the spatial distribution of noise. Global operations can be enhanced by the user to manipulate only a subset of an image histogram, but these may only involve simple truncation of the histogram or application of local filters to pixels whose values fall within the specified subset of the histogram.

## **RESPIRATORY SYNCYTIAL VIRUS**

### **History**

Respiratory syncytial virus (RSV) was isolated from a chimpanzee in 1955 [37] and was later determined to be a prominent human pathogen [38], particularly in those of the pediatric, elderly, and immunocompromised populations [39-41]. Like many disease-causing agents, the characterization of the molecular and pathological functions of this Paramyxovirus has progressed over the years with the intent of eradication from the globe by means of a cure or widespread vaccination as with smallpox [42]. Unlike other Paramyxoviruses for which we currently vaccinate children [43, 44], an effective vaccine has not been produced despite attempts with negative consequences [45]. To this end, high-resolution structural analyses may provide insight into the mechanisms used by this virus to infect a host and transmit to subsequent hosts for maintenance in the human population by uncovering the protein-protein interactions that make this virus such an efficient pathogen.

High-resolution structures derived from X-ray crystallography of a few individual proteins have been obtained in recent years [46-49], but this is out of the context of the full virus where several proteins play a role in viral ultrastructure. Previously, lower resolution visualization of whole virus particles has been attained through EM of negatively stained virus [50], SEM [51, 52] and TEM of resin-embedded sections [53, 54]. While structural information can be deciphered from these EM methods, the full 3D volume of virions cannot be discerned from a single, 2D image of a sample. Characterization of the ultrastructure of the Measles and Sendai Paramyxovirus virions has been achieved through cryo-electron tomography [55, 56], while whole-virus description of RSV particles remains unqualified. In light of this, generation of 3D tomographic volumes from tilt series of 2D images and characterization of RSV particles have been accomplished in this work.

### **Viral Replication**

The RSV genome consists of ten genes that encode for eleven proteins [57-60]. Infection of susceptible host cells is mediated by receptor binding via the attachment glycoprotein (G) and subsequent membrane fusion via the fusion glycoprotein (F) [61]. Like other Paramyxoviruses, though, F may also induce fusion with neighboring cells independent of G, resulting in the formation of syncytia, where viral genomes may spread to the cytoplasm of an uninfected cell without the potential risk of interference from the host immune system [62]. The short, hydrophobic (SH) protein is a smaller glycoprotein on the surface of RSV particles, but has been shown dispensable for productive infection, although its presence in virions does enhance viral propagation in a susceptible host [63]. Like all Paramyxoviruses, the matrix (M) protein of RSV is the primary force behind budding of particles and the overall shape of each virion [64]. The C-terminal region of M contains a membrane-binding domain like other

Mononegaviruses [48], but it also interacts with other structural proteins as a link between the membrane and the genome cargo to be transported to new cells after budding. One of these proteins, M2-1, is encoded for by the M2 gene of the RSV genome and has been shown necessary for productive transcription of the initial non-structural genes NS1 and NS2 from the 3' end of the genome and continued transcription along the length of the genome for downstream genes. The M2 gene, however, has an additional start site for the gene M2-2, which has been shown to halt RSV replication under over-expression in cell culture [60]. The remaining structural proteins – nucleocapsid (N), phosphoprotein (P), and RNA-dependent RNA polymerase (L) – interact first to create positive-sense transcripts to be used for protein translation and, when equal in length to a full genome, an antigenome template for replication of the new negative-sense strand for subsequent infections.

Once a full-length, negative-sense RNA genome is transcribed, it is then encapsidated by the ribonucleoprotein (RNP) complex consisting of N, P, and L for packaging into virions [61]. Occasionally in Paramyxoviruses, however, incomplete genomes are encapsidated with RNP and packaged into virions, resulting in defective interfering (DI) particles [65, 66], so named because the packaged genome cannot permit full-length replication in a cell with which it subsequently fuses. Once fused, however, the DI genome may replicate using the packaged N, P, L, and M2-1 proteins to generate proteins and possibly further DI genomes that can interfere with a researcher's attempt to purify high titers of viable virus particles.

Each RNP filament containing a RNA genome then interacts with M in the cell cytoplasm in inclusion bodies for eventual trafficking to the cellular membrane for budding of a progeny virion [67]. This interaction is mediated by the M2-1 protein [68], making it a dual-use protein that functions both as a transcription anti-terminator at the onset of infection and as a structural component to ensure packaging of genomic RNA at

the end of the viral replication cycle. Some Paramyxovirus M proteins have been shown sufficient for budding of virus-like particles (VLPs) without other viral proteins present [69-71], while others require additional viral proteins, such as F and/or N, for budding at maximum efficiency [64, 72, 73]. Finally, RSV M is trafficked to the apical budding surface and co-localized with F in lipid rafts to bring all of the structural components needed for a complete virus particle together [74].

### **Contribution from the Host**

As viruses are not classified as living organisms, they must utilize the molecular machinery and compounds of the host cell it infects to complete a replication cycle for generation of new virions to spread and infect new hosts for propagation of the input viral genome. As negative-sense RNA viruses but unlike Orthomyxoviruses, Paramyxoviruses replicate in the cellular cytoplasm for efficient translation of viral proteins by host ribosomes [61]. The typical processes of other host proteins, however, are also subverted by Paramyxoviruses for transcription and morphogenesis of new generations of virus particles. The matrix of Sendai virus has been shown to interact with cellular actin [75], and Measles virus particles and RSV particles have been shown to contain cellular actin [76, 77]. For human parainfluenza virus type 3 (PIV3), Sendai virus, and Measles virus, actin has been shown necessary for transcription of viral proteins by the virally encoded RNA-dependent RNA polymerase (RDRP) [78-80].

For RSV, actin contributes to both trafficking of viral components to cell membranes and transcription of the viral genome by viral RDRP. Transcription was first shown to require the presence of actin in a cell-free in vitro assay [81] and later shown to be enhanced by the cellular factor profilin [82]. RhoA, a member of the Ras GTPase superfamily, is known to modulate cellular actin [83, 84] and has been shown to interact with the F glycoprotein [84], which trafficks to the apical membrane for budding of the

virion. Additionally, RhoA and actin are important for generation of filamentous Paramyxovirus virions [53, 85] and formation of syncytia from infection of several Paramyxoviruses [84, 86-88].

### **Virus Morphology**

Budding RSV particles, to date, have been characterized predominantly as filaments of varying lengths [51, 52, 89, 90], mirroring those of Filoviruses Ebola and Marburg [91, 92], with few instances of spherical cross-sections [53, 93]. This variety of morphotypes is not surprising with respect to other Paramyxoviruses, such as Measles [55] and Sendai virus [56], as the structural hallmark of this family of viruses is its pleiomorphic nature. Several negative-sense RNA viruses have a matrix protein but cannot be described with a single morphology unlike the unique bullet shape of Rhabdoviruses [94]. Influenza, a member of the Orthomyxoviridae [95], and Lassa virus, an Arenavirus [96], contain the M1 and Z proteins, respectively, whose major function is to illicit budding of RNP-coated genomes for formation of progeny virions, and also represent pleomorphic families of RNA viruses. To delineate the truly predominant 3D morphotype of a budded particle in a cell-free context, supernatants from an infected cell culture must be visualized by electron tomography. To this end, the characterization of RSV particles visualized through cryo-electron tomography is presented through various procedures of image processing.

## CHAPTER II

### MATERIALS AND METHODS

#### *Virus Preparation*

The RSV A2 strain was cultured in Hep-2 cells under batch conditions. Virus particles were purified to a count of approximately  $6 \times 10^9$  particles per ml (TCID<sub>50</sub> titer =  $10^6$  TCID<sub>50</sub>/ml). Aliquot samples of this virus suspended in a 10mM Tris, 150 mM NaCl, 1mM EDTA, pH 7.5 buffer were obtained from Advanced Biotechnologies Inc. (Columbia, MD).

#### *Sample preparation for cryo-ET*

Four microliters of viral suspension were pipetted onto glow-discharged Quantifoil grids with application of 10nm BSA-treated or protein-A-treated colloidal gold as a fiduciary marker. Grids were then plunge frozen into liquid ethane using either a Vitrobot Mark III or IV system.

#### *Data collection*

Collection of tilt series through EM was performed on two microscopes: 1) JEOL JEM-2200FS 200KV FEG-TEM with an in-column energy filter (slit width 20 eV) and a 4k x 4k Gatan Ultrascan CCD camera at Emory's Robert P. Apkarian Integrated Electron Microscopy core; 2) an FEI Titan Krios 300kV FEG-TEM with a GIF-2002 energy filter (slit width 20 eV) and a 4k x 4k Gatan Ultrascan CCD camera at Rocky Mountain Laboratories, Hamilton, MT. Images were collected with pixel sizes of 0.446nm on the specimen. The total electron dose of  $120 \text{ e}^-/\text{\AA}^2$  was fractionated over individual tilt series ranging from  $-62^\circ$  to  $+62^\circ$  of tilt. Defocus on the specimens ranged from 4 to 6  $\mu\text{m}$  under focus. Tilt series images were collected automatically by Drs. Wright, Holl, Guerrero-



Ferreira and Nair with tilt angle increments of  $2^\circ$  by using either SerialEM [97] or the FEI Tomography package.

### *Image processing*

Raw 16-bit tilt series were first modified in Bsoft [26] to adjust the pixel values from all negative values (i.e. signed) to all positive values (i.e. unsigned) to avoid errors in subsequent Fourier transform based reconstruction. Unsigned tilt series were then reconstructed into tomograms using R-weighted back-projection in IMOD [22].

Denoising consisted of the use of a bilateral filter [34] in Bsoft [26] (space sigma = 1, range sigma = 5 times raw dataset standard deviation, kernel size = 3x3), mean and median filters in Amira (Visage Imaging GmbH), or voxel averaging along the Z-axis of each tomogram in IMOD [22]. Graphical analysis was performed in either Excel or Prism (GraphPad software).

Denoising: Denoising algorithm development consisted of standard mean and median filters. Each method was run using a three-by-three (3 x 3) sliding window for 2D denoising and a 3 x 3 x 3 sliding window for 3D denoising operations with dimensionality at the user's discretion. These statistical methods were sometimes augmented with a selectivity condition that only applied the denoising operation if the central pixel (for 2D) or voxel (for 3D) value was a unique maximum or minimum as compared to the other integer values in the window. At each iteration, signal-to-noise ratio (SNR) was calculated as the window's mean divided by its standard deviation. Edges were handled by surrounding each dataset with a single pixel wide border of gray value around each slice of the tomogram such that the central peak subject to alteration would be derived from the dataset itself. Before processing, the histogram of the 3D volume was equalized on the respective 8- or 16-bit scale to enhance initial contrast according to the dimensionality chosen by the user.

TubeTracker: The feature tracking through tomogram volumes algorithm, TubeTracker, was designed as a C++ module for Amira (Visage Imaging) to follow continuous structures, especially RNP helix tubules, through a user-defined number of iterations, where the points in the feature's trajectory were determined by the maximal cross-correlation of a series of tangent planes generated from each previous point at angles ranging  $\pm 45^\circ$  in the XZ plane ( $\theta$ ) and the YZ plane ( $\psi$ ) about a central point, P. The unit changes to populate a 2D tangent plane from  $\theta$  and  $\psi$  proceeded according to the following formulae:  $dx = P_x + \sin(\theta)$ ;  $dy = P_y + \sin(\psi)$ ; and  $dz = P_z + \cos(\theta)\cos(\psi)$ . The remaining user-defined ports and variables are as follows: 1) Radio box for selection of tangent planes or tangent volumes; 2) Choice of output volume type of raw tangent planes or rotational averages; 3) User-defined diameter of tube to track; 4) Lensing method to apply to each tangent plane before cross-correlation with choices "None", "Spherical", and "Gaussian", weighting the values by a kernel of dimensions equal to the plane to each choice; 5) Increment by which to vary the axial angle in degrees; 6) Angular increment for creation of a rotationally averaged tangent plane; 7) Vector length by which to create tangent planes for a point at each iteration; 8) Integer by which to sample input dataset such that the sampling distance between points is the reciprocal of the integer value entered; 9) Boolean to indicate full  $45^\circ$ -by- $45^\circ$  search range or only the cardinal axes as two separate phases to speed up calculation; 10) Boolean to indicate if dataset values should be inverted about its respective bit-level such that dark pixels representing density will have a higher value for calculation of the center of mass of each central plane at each iteration; and 11) Boolean to indicate of each tangent plane should be normalized to a Gaussian distribution with a mean of zero and a standard deviation of 1. To minimize deviations from the true trajectory, each iteration was concluded with a center of mass calculation to place the center of the tubular cross-section at the center of the 2D tangent plane image. Point coordinates were stored as

arrays of length equal to the number of iterations specified by the user. Output from this module consisted of a “LineSet” object made from the points stored in the coordinate arrays and a 3D image, with each 2D slice consisting of the cross-section that maximally correlated with the original 2D slice.

## CHAPTER III

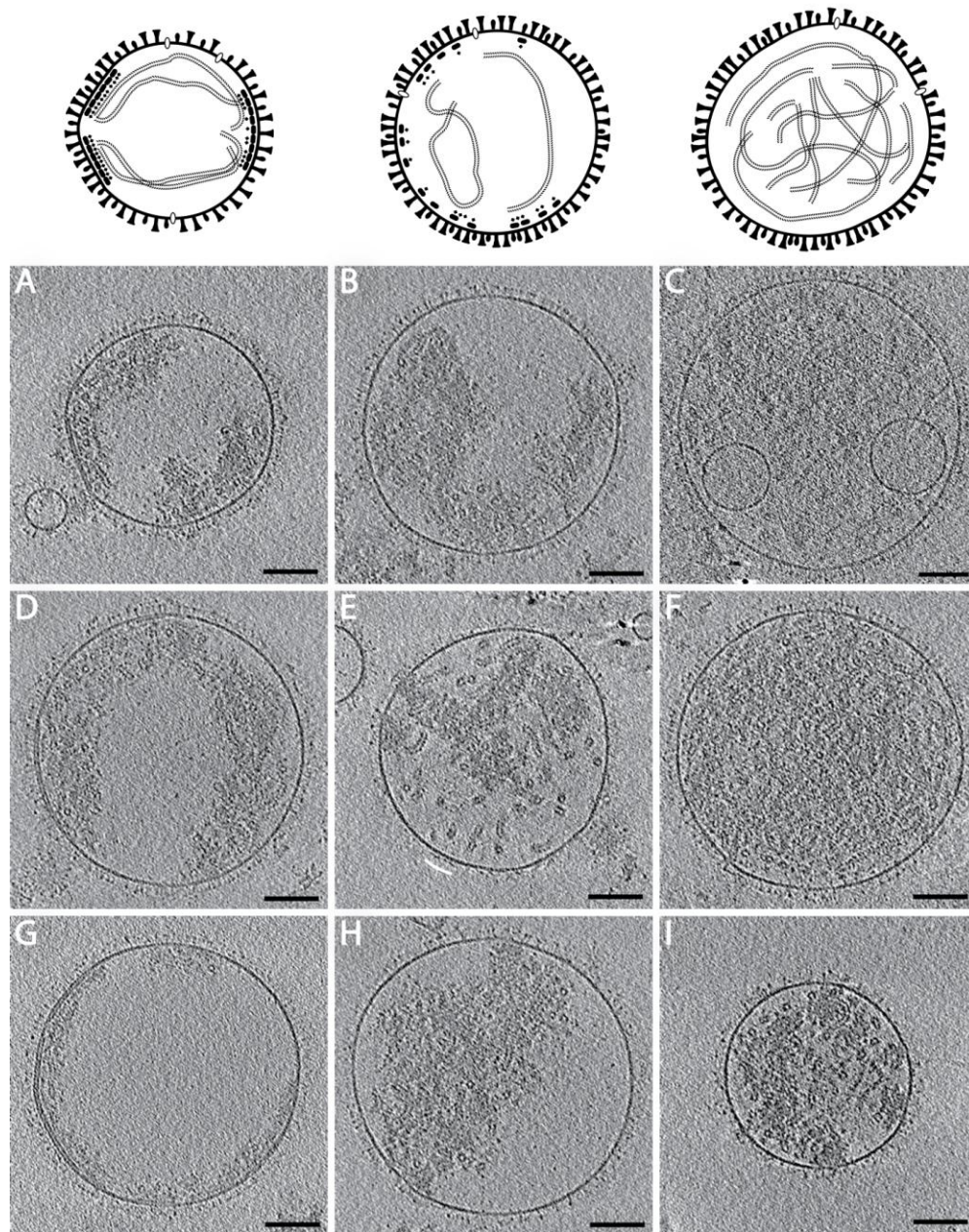
### RESULTS

#### RSV Morphology

Figure 1 shows a gallery of particles as classified by the presence of their respective structural components visible in 2D slices of the XY plane. Designation of particles into Group 1 (Fig. 1A, D, and G) was dependent on the visualization of a defined matrix (M) layer interior to the viral membrane. In each particle analyzed, the layer of M did not fully cover the interior surface of the membrane for any 2D cross-section, but rather appeared as a single oligomeric patch or broken, disjointed patches spread unevenly around the virus. With Group 2 viruses (Fig. 1B, E, and H), however, no visible layer could be distinguished as distinct from the membrane. Similarly, Group 3 viruses (Fig. 1C, F, and I) had no visible layer of density interior to the membrane that would indicate the presence of M. Groups 2 and 3 did differ by the density of ribonucleoprotein within each virion with Group 2 viruses containing a more disperse array of herringbone structural density, indicative of a standard Paramyxovirus helical ribonucleoprotein (RNP), and Group 3 viruses being fully packed with RNP such that separation between strands was difficult to distinguish. Images were averaged by five slices along the viewing axis (i.e. Z dimension) for enhanced contrast and clarity of structural features with respect to background noise and variation in surrounding densities not related to material derived from the virus, such as the suspension media.

The morphotypes for this Paramyxovirus purified from the supernatant of batch cultures was mostly spherical with an X to Y axial ratio of 1.013. While the X-Y cross-section yielded circular morphology, the Z dimension was smaller, due to compression of the ice layer surrounding each particle. Common to all viruses, as seen in Figure 1, the F and G glycoproteins extended from the surface in varying concentrations around each

particle, sometimes clumping into groups of like height (Fig. 1E, white curve). Elongated glycoproteins were the most abundant of the two in all cases.

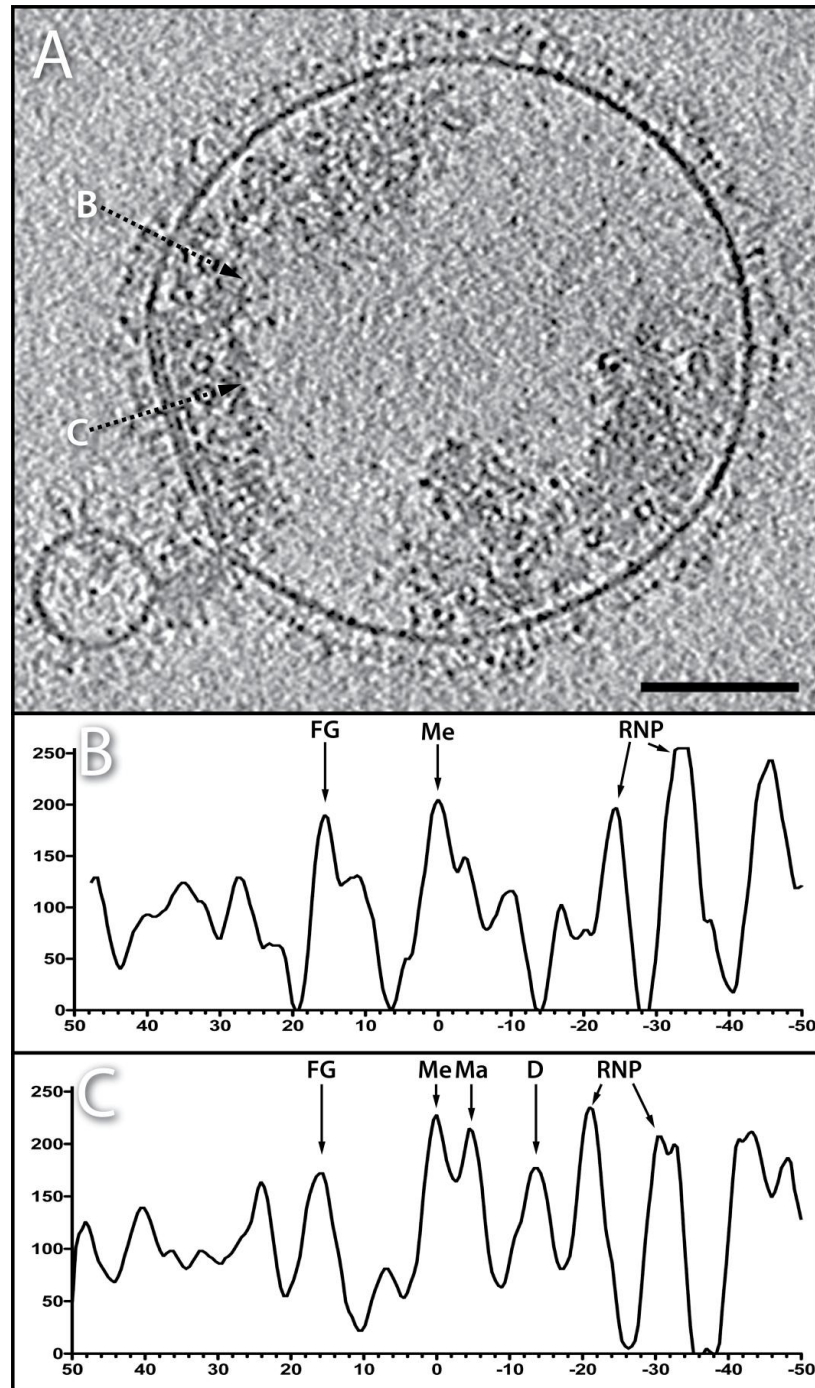


**Fig. 1: Three groups of RSV particles classified by structural densities present in 2D cross-sections of tomograms**

RSV particles in Group 1 (A, D, and G) contain a second layer of density around the periphery of virions independent of the membrane, representing matrix protein oligomers. Virions in Groups 2 (B, E, and H) and 3 (C, F, and I) had no visible layer of matrix but differed from each other by relative concentration of RNP densities within. Models for each group are presented in top row. Scale bar = 100nm.

With Group 1 viruses, the distances between structural densities in close proximity with the membrane were quantified by means of a linear profile perpendicular to the membrane (Fig. 2). Values were inverted so that electron densities indicative of the biological specimen appeared as peaks and correlate to height on the graph as opposed to troughs, which is typical of pixel values in images. The profiles extended from a glycoprotein through the membrane down through a cross-section of RNP, giving center-to-center measurements of 15.6 nm and 16.1 nm (B and C, respectively) between the glycoproteins and membrane densities and 4.5 nm between membrane and matrix densities (C only). The RNP had a cross-sectional width of 8.9 nm and 9.6 nm (B and C, respectively), correlating with published crystal structures of nucleocapsid that measured 10 nm [49]. In the profile traversing the matrix density an additional density, D, was seen. This density appeared as a layer of points interior to M and seemed to be linking the RNP to the layer of M. The center-to-center distance between M and D was calculated to be 9nm. The smoothness of the graph can be attributed to a single use of the bilateral filter, as its usage was needed to delineate individual peak centers from surrounding noise for quantification.





**Fig. 2: Linear profile of electron densities through the RSV membrane**

A) A 2D slice of a 3D tomogram of RSV. Scale bar = 100nm.

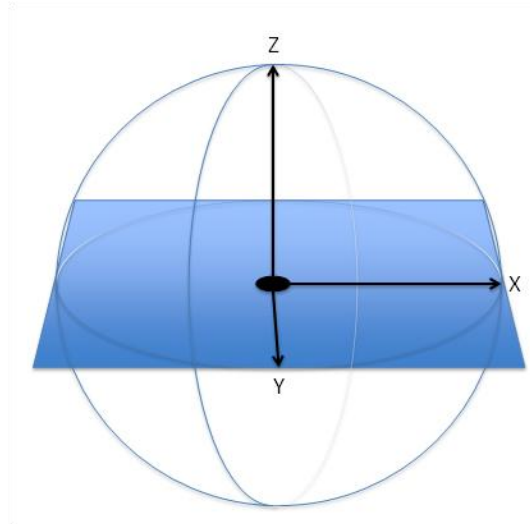
B) Inverted profile values through area without matrix, indicating densities associated with glycoproteins (FG), the viral membrane (Me), and the edges of the RNP helix cross-section. (X axis: distance from membrane, nm; positive = external, negative = internal)

C) Inverted profile values through area containing matrix (Ma), also indicating densities associated with FG and RNP as in B). An additional density, D, was visualized as well.

## Tracking of RNP

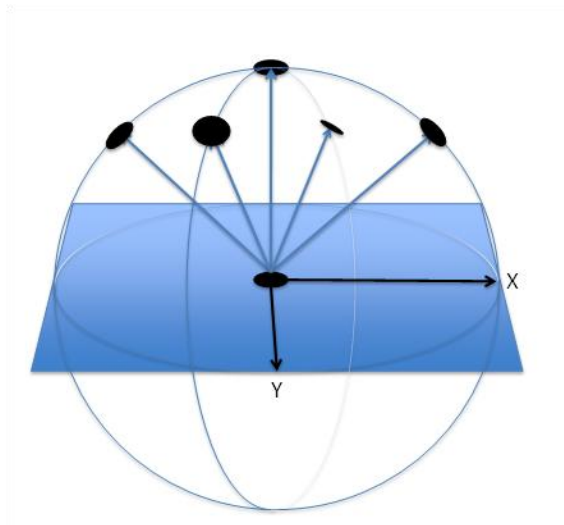
To determine the trajectory of RNP through each particle, the “TubeTracker” algorithm was developed. An initial 3D coordinate and tube diameter are input by the user along with an angular search range. As shown in Figure 3, a 2D plane is constructed at the initial point (Fig. 3A, black circle) perpendicular to the viewing direction (i.e. Z axis). From this 2D plane, a sphere of user-defined radius in pixels centered at the starting coordinate is searched for every  $\theta$  (for X-Z angles) and  $\psi$  (for Y-Z angles) at a vector length specified by the user for the user-defined angular search range, and a series of points is calculated for center coordinates of subsequent iterations (Fig. 3B). At each center coordinate, a plane tangent to the sphere is constructed as an array of float values derived from the tomographic volume through trilinear interpolation and is then cross-correlated with the starting plane to find the most likely trajectory of the tubular structure (Fig. 3C). After each search, the center coordinate of the plane exhibiting the highest cross-correlation value (i.e. closest to +1) is designated as the new center for tangent plane creation about a sphere (Fig. 3D). This procedure continues for a user-defined number of iterations.





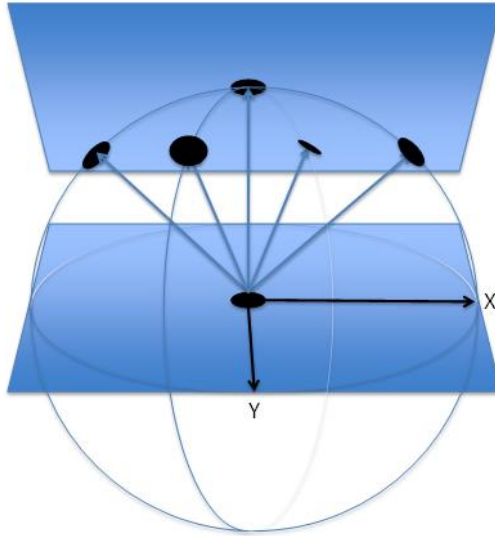
**Fig. 3A: Search sphere for generation of tangent planes**

At each iteration of TubeTracker, the center point of the current 2D plane is used as the center of a sphere. From this center point, a Z axis is determined where  $\theta$  and  $\psi$  are offset by 0 degrees from the previous iteration's trajectory vector. The X and Y axes of each plane are parallel to the X and Y axes of the dataset, respectively.



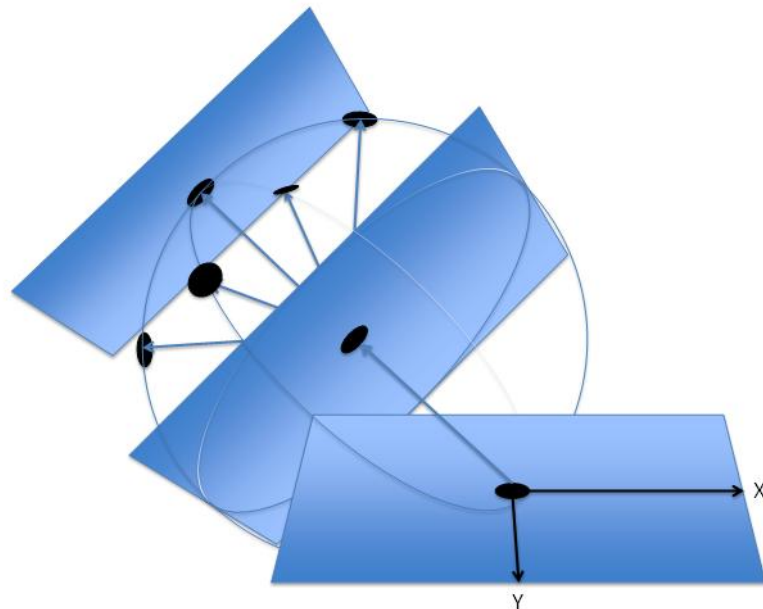
**Fig. 3B: Center coordinates for tangent plane generation along normal vectors to search sphere**

Each center coordinate for tangent planes (black circles on sphere) is generated along vectors normal to the search sphere centered at current iteration's tracked central reference point (black circle at intersection of X and Y axes). Normal vectors (blue lines) are calculated from the reference Z axis by incrementing  $\theta$  and  $\psi$  for a user-defined range by a user-defined increment.



**Fig. 3C: Tangent plane creation at center points on search sphere**

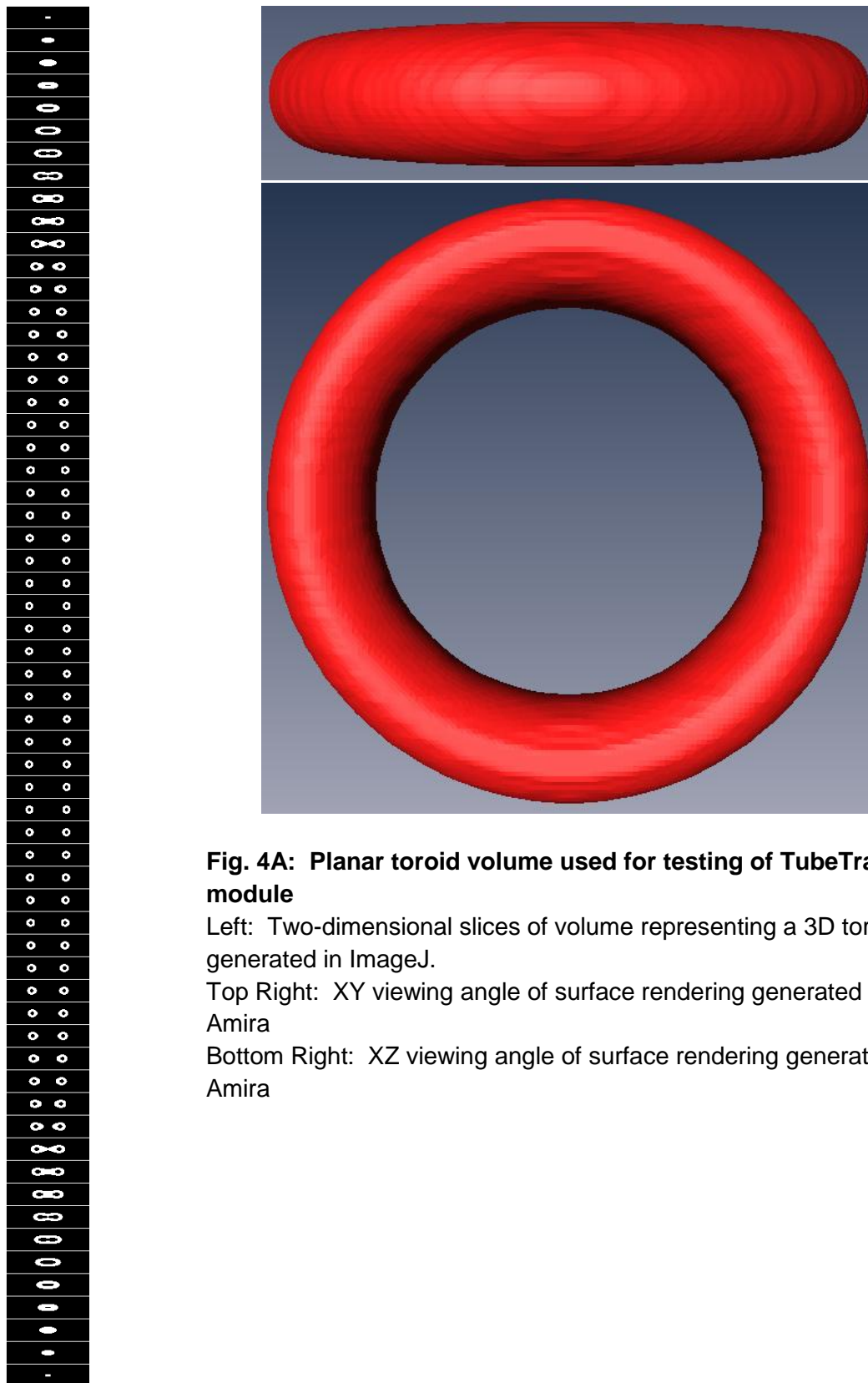
At each iteration, a plane of user-defined width and height is interpolated from the input 3D volume at an angular range of  $\pm 45^\circ$  along XZ axes ( $\theta$ ) and YZ axes ( $\psi$ ) by 3D coordinates  $\{x,y,z\} = \{\sin(\theta), \sin(\psi), \cos(\theta)\cos(\psi)\}$ .



**Fig. 3D: Creation of search sphere at center coordinate of tangent plane with best cross-correlation value**

After the first iteration, tangent planes are generated along vectors perpendicular to normal vectors of a subsequent search sphere centered at the previous iteration's center coordinate from which the tangent plane generated produced the highest cross-correlation value.

The algorithm was tested in Amira using a hollow toroid as model data (Fig. 4A). Model volumes were constructed in ImageJ as binary 8-bit images (white value = 255, black value = 0) and converted to surface renderings automatically in Amira using the “LabelVoxel” option, which allows a user to create a volume based on thresholded ranges of input data from which to generate points for triangles of a surface. The center coordinates were output as a series of 3D points with intervening distance of five voxels and connected by a line in Amira for ease of viewing the tube’s trajectory (Fig. 4B). At each center coordinate of the first iteration (i.e. the initial point chosen by the user), a montage containing each tangent plane was output as an image for verification that the chosen point was indeed a cross-section perpendicular to the viewing axis (Fig. 4C).

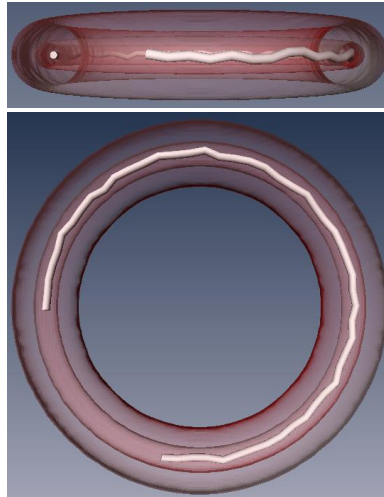


**Fig. 4A: Planar toroid volume used for testing of TubeTracker module**

Left: Two-dimensional slices of volume representing a 3D toroid generated in ImageJ.

Top Right: XY viewing angle of surface rendering generated in Amira

Bottom Right: XZ viewing angle of surface rendering generated in Amira

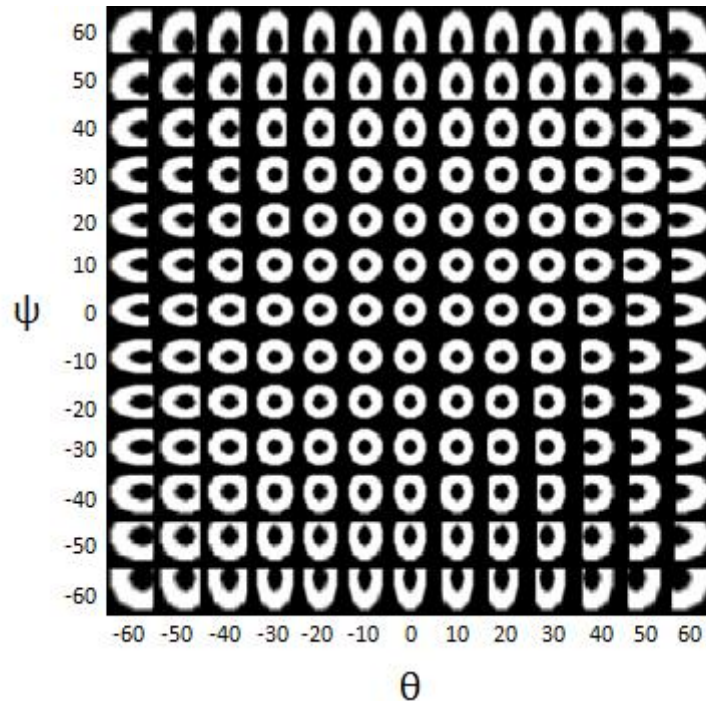


**Fig. 4B: LineSet object showing trajectory from TubeTracker for 50 iterations through transparent surfaces of 4A**

Top: XY view

Bottom: XZ view

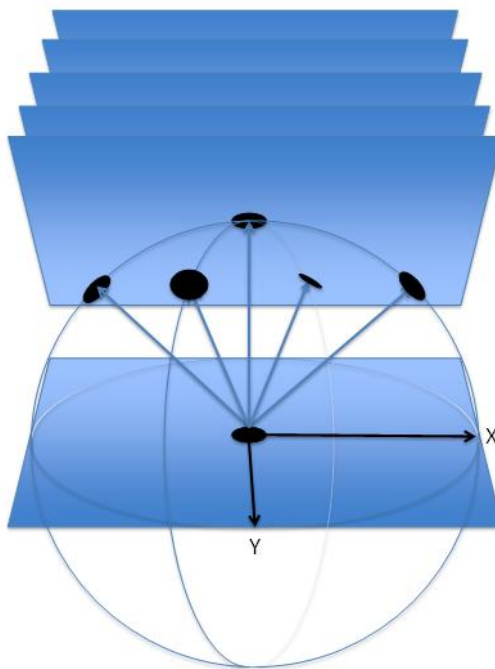
White line: Consecutive points of maximum cross-correlation values for 50 iterations



**Fig. 4C: Tangent planes of first iteration of TubeTracker usage with planar toroid**

Each tangent plane from the tube center is created along the  $\theta$  and  $\psi$  range of  $\pm 60^\circ$  with an angular increment of ten degrees. As visible here, the plane most like the cross-section of the radially symmetric tube is that at  $\theta = 0^\circ$ ,  $\psi = 0^\circ$ .

As the toroid was generated on a single plane with no shift in Y coordinates for the tube center, it was expected that only the X and Z values of center coordinates would vary. With an angular search increment of five, however, this was not the case; therefore, an option was implemented for the user to generate volumes tangent to the search sphere instead of single planes (Fig. 5). Each XY slice of the tangent volume was cross-correlated along its Z dimension, which was equal to the vector magnitude, to the starting plane and their cross-correlation values summed (i.e. cumulative cross-correlation). This yielded a reduced standard deviation ( $\sigma = 0.656$ ) from the same initially chosen Y coordinate as compared with single tangent planes ( $\sigma = 0.716$ ).



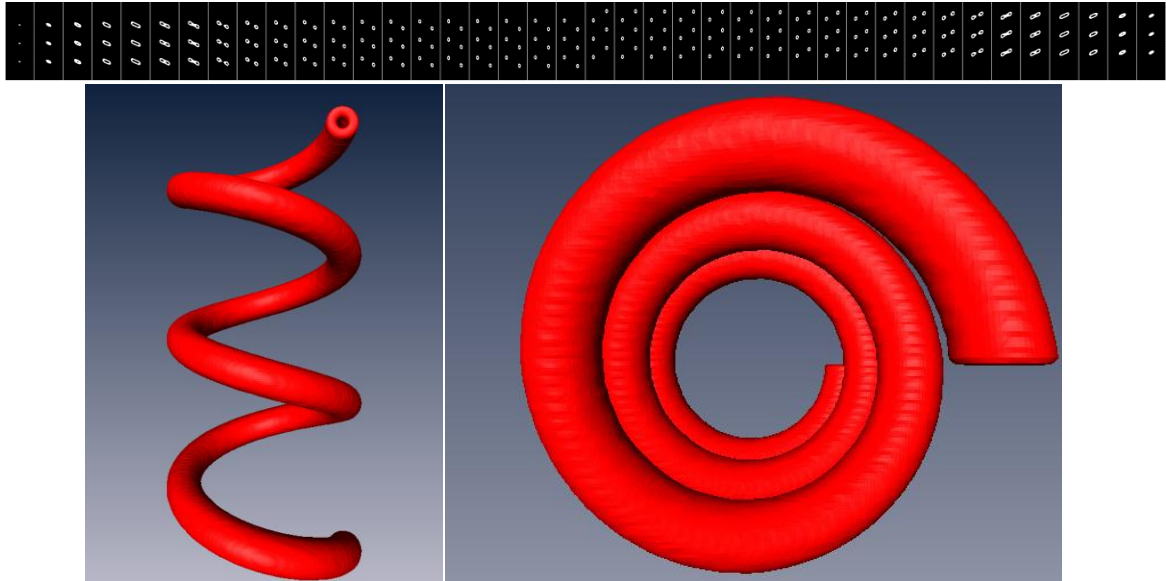
**Fig. 5: Generation of tangent volume as series of tangent planes**

Black circles: Center points for tangent plane generation

Blue lines: Normal vectors for tangent plane generation

Black lines: 2D X and Y axes orthogonal to normal vector with  $\theta = 0^\circ$  and  $\psi = 0^\circ$

TubeTracker was then tested on a helical toroid generated by the same ImageJ script that generated the planar toroid (Fig. 6A). Fifty iterations along a vector magnitude of five and a search angle increment of three produced reasonable results with the simple tangent plane method (Fig. 6B). For reasons unknown, the tangent volume method with this same angular search increment over the same search range of  $\pm 45^\circ$  did not complete the same number of iterations, but instead caused Amira to unexpectedly terminate; therefore, the search angle increment was increased to five, resulting in the creation of 1,805 (magnitude\*19<sup>2</sup>) tangent volumes instead of 4,805 (magnitude\*31<sup>2</sup>) per iteration. The results showed the same angular progression about the central axis of the helix as with the 50 iterations of the planar toroid.

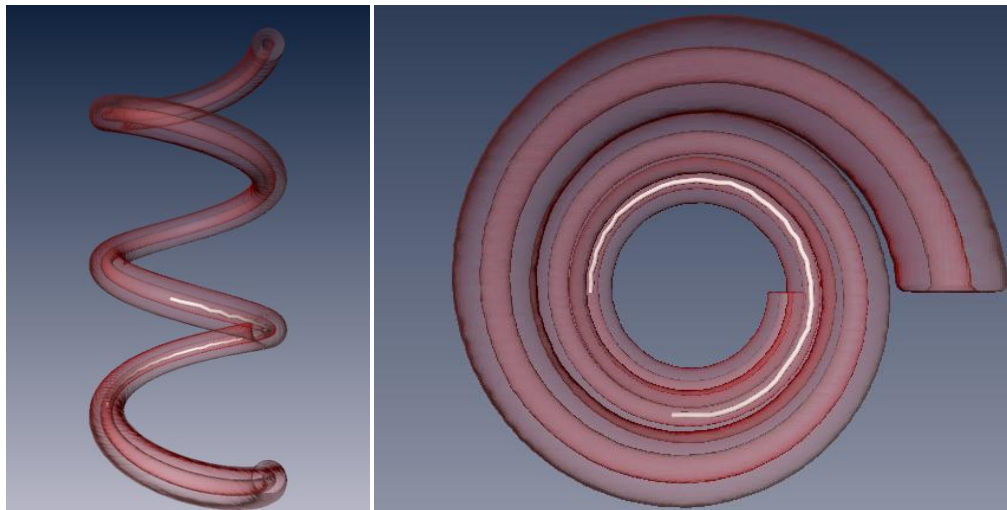


**Fig. 6A: Surface renderings of tubular helix**

Top: Two-dimensional slices of volume representing a 3D helix tube.

Bottom Left: XY view of surface rendering

Bottom Right: XZ view of surface rendering



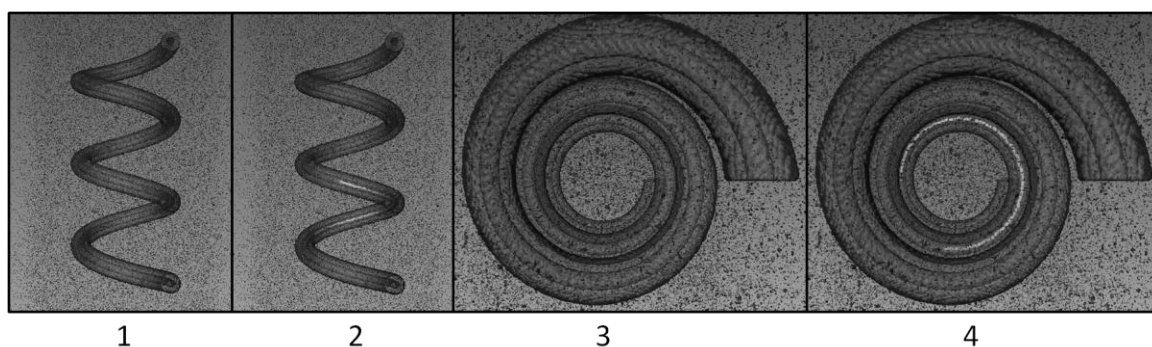
**Fig. 6B: LineSet object showing trajectory from TubeTracker performance of 50 iterations through transparent surfaces of tubular helix in 6A**

Left: XY view

Right: XZ view

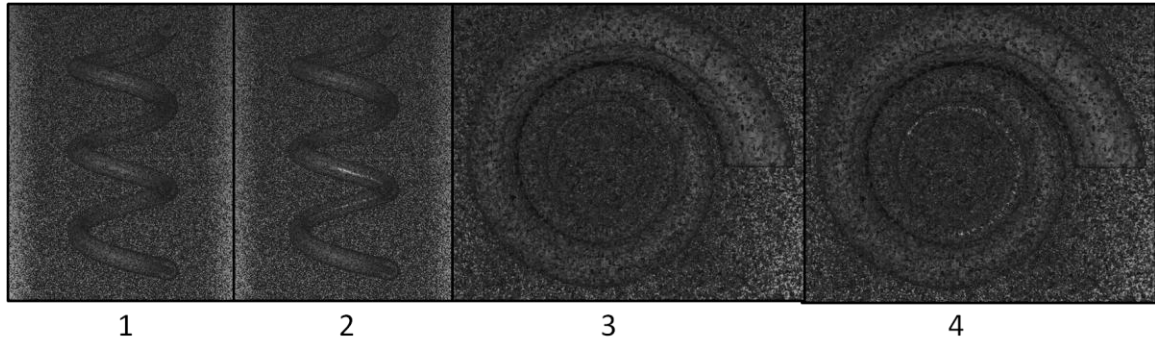


These toroids were generated for testing purposes but lacked the same speckled shot noise present in cryo-electron tomograms. To this end, noise was added to the helical toroid in ImageJ in two stages and tested further. After a single addition of speckled noise in ImageJ, TubeTracker was able to perform similarly to the noise-free volume with the same user-defined variables Fig. 7A). Two additions of speckled noise also had minimal influence on the tracking accuracy (Fig. 7B).



**Fig. 7A: TubeTracker performance of 50 iterations on tubular helix of Fig. 6 with one addition of speckle noise**

- 1) XY view of helix isosurface rendering from 1.
- 2) XY view of helix isosurface rendering from 1 with LineSet showing TubeTracker performance for 50 iterations.
- 3) XZ view of 1.
- 4) XZ view of 2.



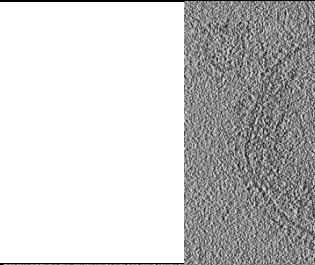
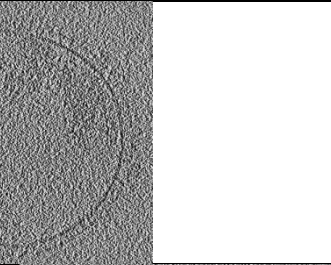
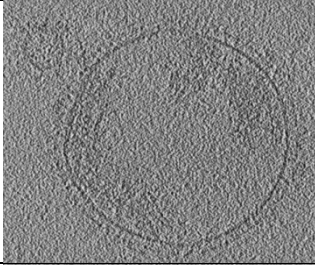



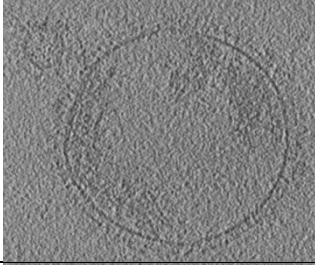

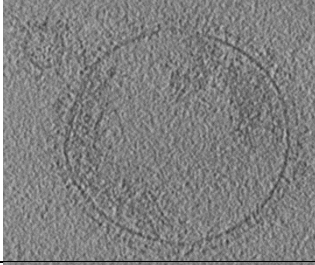
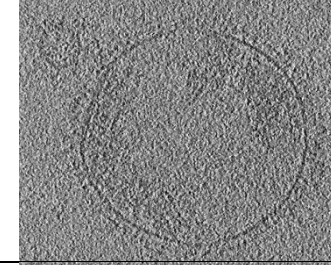
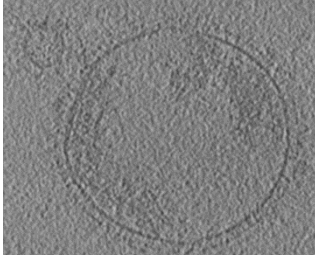

**Fig. 7B: TubeTracker performance of 50 iterations on tubular helix of Fig. 6 with two additions of speckle noise**

- 1) XY view of helix isosurface rendering from 1.
- 2) XY view of helix isosurface rendering from 1 with LineSet showing TubeTracker performance for 100 iterations.
- 3) XZ view of 1.
- 4) XZ view of 2.

With these results in hand, TubeTracker was run on a raw RSV tomogram after reconstruction in IMOD. The module initially progressed similarly to the toroid model volume but after a nominal number of iterations becomes skewed from the true RNP trajectory. As electron density presents itself as darker voxel values, which are closer to zero on an 8-bit scale, the pixel values of the tomogram were inverted so that electron density would now appear white as in the model toroids. This too, however, did not accurately trace the path of the RNP tubes. It was concluded that additional denoising steps may be necessary even with the results of the additive noise of the model tomograms. After the use of several local filters, these results remained unchanged. The application of global filters, too, was unsuccessful in enhancing the tracking of RNP tubules. This may be due to an additional need not yet present in the algorithm to optimize the initial vector at the user-defined starting coordinate so that it is indeed started as a true cross-section of a tube.

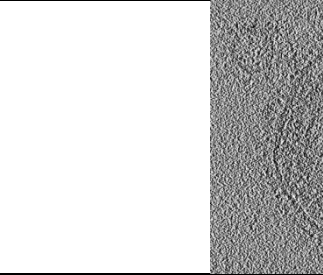
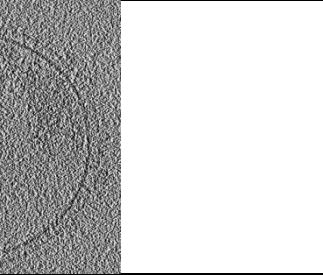
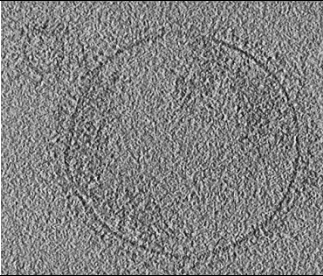
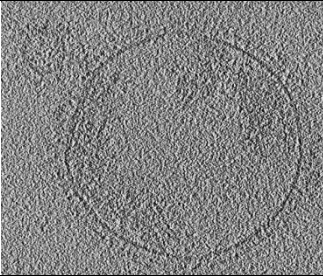
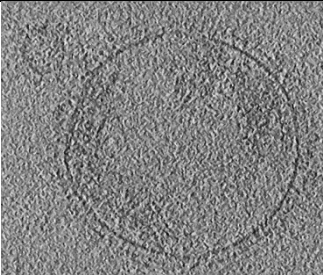
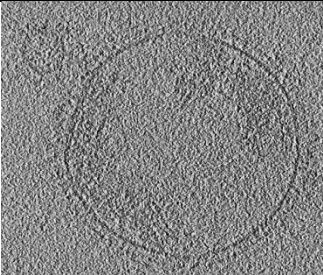


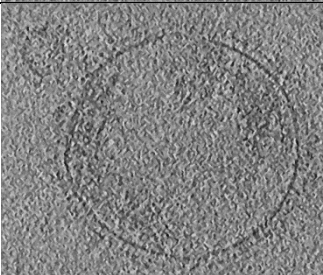
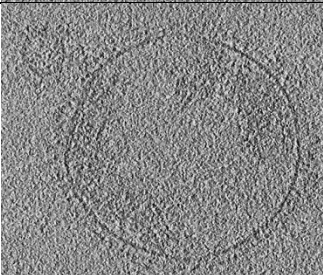
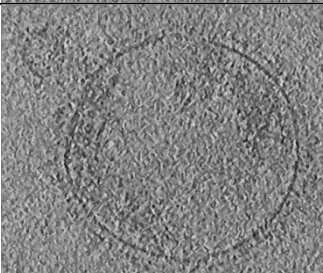

### **Noise Reduction in RSV Tomograms**

Attempts to reduce the interference of noise present in RSV tomograms were performed through the use of 2D three-by-three (3x3) local filters, including mean, median, and bilateral, from one to five iterations. For minimization of smearing of signal, the mean and median filters were applied alongside their selective versions, which only altered the center pixel if it was found to be a unique maximum or minimum value in the 3x3 sliding window (Fig. 8A and B, respectively). These results were compared with the bilateral filter over five iterations (Fig. 8C) by means of a SNR calculation (Fig. 8D). The SNR value rose most quickly with filters that changed the center pixel to an averaged value, whether weighted with the bilateral filter or unweighted with the mean filter. The SNR slope was smallest with the selective filters over five iterations.

Iteration	3x3 Mean	3x3 Selective Mean
0 (Raw data)		
1		
2		
3		
4		
5		


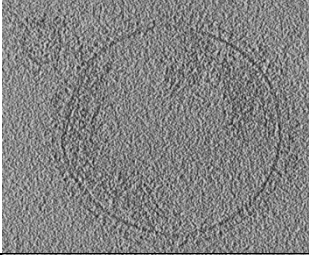


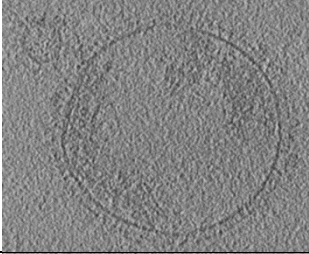
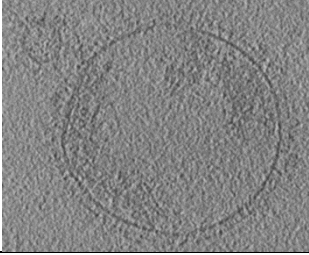
**Fig. 8A: 3x3 Mean filter vs. 3x3 Selective Mean filter**

A 3x3 mean filter over-smoothes the tomogram slice much more rapidly than its selective version, which retains coherent separation between the membrane and matrix layers over more iterations by comparison.

Iteration	3x3 Median	3x3 Selective Median
0 (Raw data)		
1		
2		
3		
4		
5		

**Fig. 8B: 3x3 Median filter vs. 3x3 Selective Median filter**

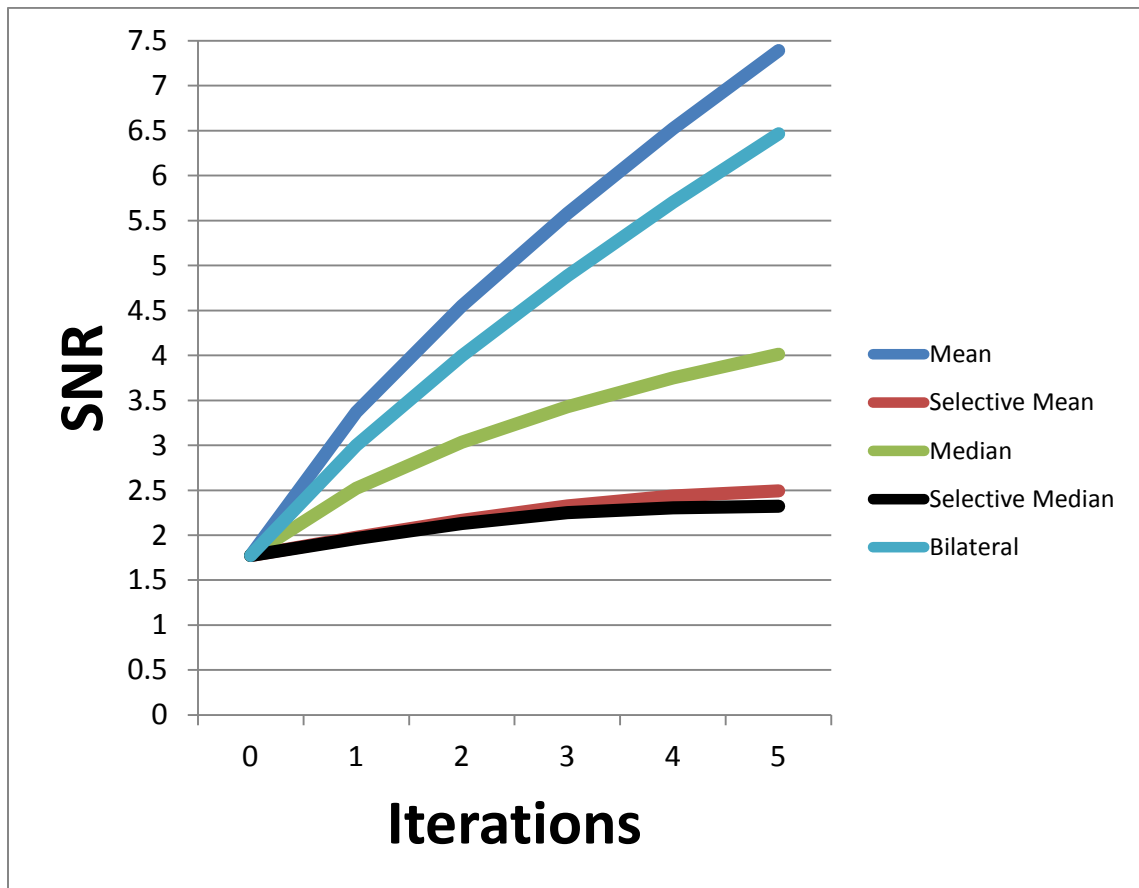
Application of a 3x3 median filter shows more rapid smoothing than its selective counterpart. Distinction between the membrane and matrix layers diminishes more slowly with the use of the selective median filter.

Iteration	3x3 Bilateral
0 (Raw data)	
1	
2	
3	
4	
5	



**Fig. 8C: 3x3 Bilateral filter**

Application of a 3x3 bilateral filter shows rapid smoothing over five iterations with three iterations seeming to remain the least smeared while retaining relevant structural information.



**Fig. 8D: SNR measurements for five iterations of mean, median, and bilateral filters**

After five iterations, selective application of the mean and median filters showed slower rise in SNR measurement than non-conditional application. The mean filter showed fastest increase in mean to standard deviation ratio, and the bilateral filter has the next highest rate of increase, indicating that a simple average or weighted average is most effective at improving the SNR of a dataset.

## CHAPTER IV

### DISCUSSION

Cryo-ET is a proven method to characterize the structural components of macromolecular assemblies and whole pleiomorphic viruses at the nanometer level scale in their native state [55, 56, 91, 94, 95]. With respect to RSV, this technology has never been applied, leaving current perceptions of RSV morphology and relative structural component orientations of limited value beyond a conceptual level. By using this method to classify this virus according to its structural densities, the study presented here shows that the overall morphology of RSV derived from purification of viral supernatants may not necessarily be locked into a single morphotype, confirming the pleiomorphic nature of this Paramyxovirus. This lack of rigidity in viral proteins typically classified for structural integrity – namely the matrix protein – seems to allow for the most thermodynamically stable conformation of spheres in an aqueous solution.

The undefined density, D, seen in several tomograms analyzed (Fig. 2C), may be the Pneumovirus-specific M2-1 protein. This hypothesis is substantiated by previous work showing both its interaction with matrix and its binding capacity to the helical RNP complex [67, 98]. Should this idea be confirmed by other experiments, such as immun-EM of sectioned virus particles, it would confirm a structural function for M2-1 beyond its already characterized transcriptional and translational activities.

The TubeTracker module presented here shows promise in elucidation of tubular structural components in cryo-ET. Its benefits lie in the simplicity of proven cross-correlation methods given an a priori knowledge of a starting position for the structure of interest. Additionally, this knowledge gives a user speed in analyzing continuous densities unlike other methods which compare the complete 3D volume to a model tube [99]. The test cases for this project were created as hollow tubes to model the RNP of

RSV, but the cross-correlation mechanism lends itself to potentially tracking other continuous densities, such as bacterial flagellum.

The cost of this algorithm's accuracy comes with the speed in processing the creation and cross-correlation of each tangent plane interpolated from the raw tomogram in the search for the RNP trajectory. The helical nature of the RNP may also disrupt tracking accuracy. To overcome this, it may prove useful to compress the tangent volumes into single 2D projections. This would differ from simple averaging along the direction normal to the search sphere around each point along the RNP trajectory by weighting the average radially such that the resultant tangent plane more resembles those of the model toroids. Radial weighting of the average along each search angle would require additional a priori knowledge of the pitch to the RNP helix relative to the pixel spacing in the raw tomogram, but this information has been shown for RSV to be 70Å, resulting in ten nucleocapsid subunits per turn [49]. As the module employs trilinear interpolation to fill tangent plane pixel values, this would be possible. As the helical nature could then be represented accurately as a plane, the series of tangent planes output as a volume from this module may be used alongside Fourier-Bessel approaches for helical reconstruction to perform an in-place enhancement of the resolution of RNP in the tomogram.

### Interference of Noise

Structural analysis of tomographic volumes is hampered by the initial presence of punctate shot noise in the 2D images collected as a tilt series from the microscope then reconstructed into the final 3D volume by R-weighted Fourier back projection. In this study, noise was dealt with post-reconstruction, as resolution in the tomogram suffers if the raw data is manipulated before the final volume is created. This noise that remains in the datasets used for analysis with TubeTracker interfered with determining

trajectories of the tubular RNP molecules by contributing to a detriment in cross-correlation value at each iteration because of the variance in the surrounding non-RNP densities. For this reason, denoising operations may need to occur alongside the use of TubeTracker such that each tangent plane produced is denoised before cross-correlating with the initial cross-section chosen by the user.

If the shot noise in the tilt series is not handled before reconstruction into a tomographic volume, as with the data presented here, the resulting noise in three dimensions presents itself as a small volume of noise rather than a single voxel that differs from its 27 neighboring voxels, or connected neighbors [100, 101]. To overcome this stipulation, an algorithm that progressively discriminates voxels as noise or signal based on an increasing sub-volume size may prove useful. The caveat with this approach would be to establish a threshold size maximum that would prevent true densities derived from viral proteins from being inappropriately removed or smoothed away while still removing interfering densities in the surrounding milieu of supernatant media and internal volume of the virus. The algorithm may then delineate larger structures of interest from those fragments of indescribable density in the milieu of supernatant media. This method would, in theory, distinguish a low variability background of pixel values from much smaller regions that deviate from this background by an increasing radius approach over several iterations. If successful, a threshold would be reached at the boundaries of structurally relevant densities, leaving relevant biological structures untouched while removing the unwanted interfering densities in the surrounding volume.

The selective application of the common local mean and median filters to extreme pixels in a 3x3 window showed enhancement over their usage without consideration to the nature of the pixel's local environment. By limiting their use to pixels that are the most extreme with reference to their neighbors, smoothing is lessened over

the same number of iterations. Its rate of increase in SNR by the definition presented here, however, is also lessened. As SNR was defined as the ratio of an image's mean to its standard deviation, it makes sense that the mean filter would increase the SNR value most quickly over other methods, as seen in these results. The bilateral filter, too, demonstrates a rapid increase in SNR. Since it is a Gaussian weighted mean filter that includes the central pixel's relationship to its neighbors in terms of both distance and pixel value, it can be thought of as a simple mean filter with a kernel that varies over its X and Y coordinates rather than a uniform contribution of each pixel in the neighboring window.

As the median filter uses existing values present in the 3x3 window to fill the center pixel instead of an average of surrounding pixels' values, its rate of increase in measurement of SNR is slower than that of rote averaging mechanisms. Its smoothing, though, is also relatively slow as compared to these methods. This indicates that the median filter allows a user to adjust the level of its use to a number of iterations that provides adequate smoothing of structural densities without blurring the distinction between adjacent features.

The advantage of these selective filters is their ability to tune their application to the user's needs for clarity of viral structural densities versus background noise in electron tomograms. Currently, the only criterion for use of a selective filter is whether or not a pixel is a unique minimum or maximum value when compared to its 8-connected neighbors. Beyond the simple limit of a maximum number of iterations, the filters will not affect the same pixel upon consecutive iterations because the pixel will no longer be an extreme value in its local neighborhood. The number of extreme values in a 3x3 neighborhood will diminish, then, with successive iterations, leading to a limit inherent in the algorithm's design such that denoising will no longer occur in 2D slices of a 3D volume once the number of local extreme values reaches zero. This number of

iterations would be reached more quickly by the selective median filter than the selective mean filter as new values are not generated during its application. If this extreme value limit is reached before the user decides that denoising is complete, then it may prove useful to repeat the application with a five-by-five denoising window using the same limits.

### Improvements in TubeTracker

The algorithm currently used for TubeTracker stems from established mathematical methods for aligning image subsections to their respective locations in the image as a whole through cross-correlation. It is reasonable that smaller angular increments for creating tangent planes against the search sphere would increase the likelihood of achieving a better trajectory, so this port for the module should be converted from integer valued input to float values, allowing for decimal-level incrementing for  $\theta$  and  $\psi$  in tangent plane creation. Potential memory issues may be overcome by implementing a function to update an existing plane with new values to avoid creation and deletion issues that may be present with the current programming. The center of mass calculation has been improved from integer to float accuracy but is not applied to the initial plane created at the user-defined starting coordinate. Using this function on the starting plane may improve the trajectory by centering the tubular cross-section before subsequent cross-correlation occurs that would favor an orientation that is at an unfavorable angular offset. This function, however, would require the input tomogram to be inverted so that structural density of interest contributes more to the centering than the surrounding noise and non-structural information.

## REFERENCES

1. Slonczewski J, Foster JW (2009) *Microbiology : an evolving science*. W.W. Norton & Co., New York
2. Bozzola JJ, Russell LD (1999) *Electron microscopy : principles and techniques for biologists*. Jones and Bartlett, Sudbury, Mass.
3. Claude A, Fullam EF (1945) An Electron Microscope Study of Isolated Mitochondria : Method and Preliminary Results. *J Exp Med* 81: 51-62.
4. Luft JH (1956) Permanganate; a new fixative for electron microscopy. *J Biophys Biochem Cytol* 2: 799-802.
5. Sabatini DD, Bensch K, Barnett RJ (1963) Cytochemistry and electron microscopy. The preservation of cellular ultrastructure and enzymatic activity by aldehyde fixation. *J Cell Biol* 17: 19-58.
6. Lickfeld KG, Achterrath M, Hentrich F, Kolehmainen-Seveus L, Persson A (1972) The fine structure of *Pseudomonas aeruginosa* as analyzed by freeze etching, ultramicrotomy, and cryo-ultramicrotomy. *J Ultrastruct Res* 38: 27-45.
7. Thornell LE, Sjoström M (1975) The myofibrillar M-band in the cryo-section-analysis of section thickness. *J Microsc* 104: 263-269.
8. Ali SY, Wisby A (1975) Mitochondrial granules of chondrocytes in cryosections of growth cartilage. *Am J Anat* 144: 243-248. doi: 10.1002/aja.1001440209
9. Ali SY, Gray JC, Wisby A, Phillips M (1977) Preparation of thin cryo-sections for electron probe analysis of calcifying cartilage. *J Microsc* 111: 65-76.
10. Frederik PM, Busing WM (1981) Strong evidence against section thawing whilst cutting on the cryo-ultratome. *J Microsc* 122: 217-220.
11. Frederik PM, Busing WM (1981) Ice crystal damage in frozen thin sections: freezing effects and their restoration. *J Microsc* 121: 191-199.
12. Dubochet J, McDowell AW, Menge B, Schmid EN, Lickfeld KG (1983) Electron microscopy of frozen-hydrated bacteria. *J Bacteriol* 155: 381-390.
13. Pryde JA, Jones GO (1952) Properties of Vitreous Water. *Nature* 170: 685-688.
14. Costello MJ (1980) Ultra-rapid freezing of thin biological samples. *Scan Electron Microsc*: 361-370.
15. Gonzalez RC, Woods RE (2008) *Digital image processing*. Prentice Hall, Upper Saddle River, N.J.
16. Klug A, Caspar DL (1960) The structure of small viruses. *Adv Virus Res* 7: 225-325.

17. Feng J (2012) A novel iterative solution to the phase problem. *Acta Crystallographica Section A* 68: 298-300. doi: doi:10.1107/S0108767311052561
18. Cooley J, Tukey, JW (1965) An algorithm for the machine calculation of complex Fourier series. *Mathematics of Computation* 19: 297-301.
19. De Rosier DJ, Klug A (1968) Reconstruction of Three Dimensional Structures from Electron Micrographs. *Nature* 217: 130-134.
20. Crowther RA (1971) Procedures for three-dimensional reconstruction of spherical viruses by Fourier synthesis from electron micrographs. *Philos Trans R Soc Lond B Biol Sci* 261: 221-230.
21. Dover SD, Elliott A, Kernaghan AK (1981) Three-dimensional reconstruction from images of tilted specimens: the paramyosin filament. *J Microsc* 122: 23-33.
22. Kremer JR, Mastronarde DN, McIntosh JR (1996) Computer visualization of three-dimensional image data using IMOD. *Journal of structural biology* 116: 71-76. doi: 10.1006/jsbi.1996.0013
23. Ludtke SJ, Baldwin PR, Chiu W (1999) EMAN: semiautomated software for high-resolution single-particle reconstructions. *Journal of Structural Biology* 128: 82-97. doi: 10.1006/jsbi.1999.4174
24. Frank J, Radermacher M, Penczek P, Zhu J, Li Y, Ladjadj M, Leith A (1996) SPIDER and WEB: processing and visualization of images in 3D electron microscopy and related fields. *J Struct Biol* 116: 190-199. doi: S1047-8477(96)90030-1
25. van Heel M, Harauz G, Orlova EV, Schmidt R, Schatz M (1996) A new generation of the IMAGIC image processing system. *J Struct Biol* 116: 17-24. doi: S1047-8477(96)90004-0
26. Heymann JB (2001) Bsoft: image and molecular processing in electron microscopy. *Journal of Structural Biology* 133: 156-169.
27. Lee E, Fahimian BP, Iancu CV, Suloway C, Murphy GE, Wright ER, Castaño-Díez D, Jensen GJ, Miao J (2008) Radiation dose reduction and image enhancement in biological imaging through equally-sloped tomography. *Journal of Structural Biology* 164: 221-227. doi: 10.1016/j.jsb.2008.07.011
28. Mooney PE, G. Y. Fan, C. E. Meyer, K. V. Truong, D. B. Bui, and O. L. Krivanek (1990) Slow-scan CCD camera for transmission electron microscopy. *Proc XIIth Int'l Cong Elec Microsc*: 164-165.
29. Smith S (1997) *The Scientist and Engineer's Guide to Digital Signal Processing*
30. Jiang W, Baker ML, Wu Q, Bajaj C, Chiu W (2003) Applications of a bilateral denoising filter in biological electron microscopy. *J Struct Biol* 144: 114-122. doi: S1047847703002053 [pii]



31. Hoppe W, Hegerl R (1981) Some remarks concerning the influence of electron noise on 3D reconstruction. *Ultramicroscopy* 6: 205-206.
32. McEwen BF, Downing KH, Glaeser RM (1995) The relevance of dose-fractionation in tomography of radiation-sensitive specimens. *Ultramicroscopy* 60: 357-373. doi: 0304399195000828 [pii]
33. Collins T (2007) ImageJ for microscopy. *BioTechniques* 43: S25-S30. doi: 10.2144/000112517
34. Tomasi C, Manduchi R (1998) Bilateral filtering for gray and color images. *Computer Vision, 1998 Sixth International Conference on*, pp. 839-846.
35. O'Gorman L, Sammon MJ, Seul M (2008) Practical algorithms for image analysis : description, examples, programs, and projects. Cambridge University Press, Cambridge ; New York
36. Frangakis AS, Hegerl R (2001) Noise reduction in electron tomographic reconstructions using nonlinear anisotropic diffusion. *Journal of Structural Biology* 135: 239-250. doi: 10.1006/jsbi.2001.4406
37. Morris JA, Blount RE, Savage RE (1956) Recovery of Cytopathogenic Agent from Chimpanzees with Goryza. *Proceedings of the Society for Experimental Biology and Medicine Society for Experimental Biology and Medicine (New York, NY)* 92: 544-549. doi: 10.3181/00379727-92-22538
38. Chanock RM, Parrott RH, Cook K, Andrews BE, Bell JA, Reichelderfer T, Kapikian AZ, Mastrota FM, Huebner RJ (1958) Newly Recognized Myxoviruses from Children with Respiratory Disease. *New England Journal of Medicine* 258: 207-213. doi: doi:10.1056/NEJM195801302580502
39. Hall CB, Powell KR, MacDonald NE, Gala CL, Menegus ME, Suffin SC, Cohen HJ (1986) Respiratory Syncytial Viral Infection in Children with Compromised Immune Function. *New England Journal of Medicine* 315: 77-81. doi: doi:10.1056/NEJM198607103150201
40. Dowell SF, Anderson LJ, Gary HE, Erdman DD, Plouffe JF, File TM, Marston BJ, Breiman RF (1996) Respiratory Syncytial Virus Is an Important Cause of Community-Acquired Lower Respiratory Infection among Hospitalized Adults. *Journal of Infectious Diseases* 174: 456-462. doi: 10.1093/infdis/174.3.456
41. Falsey AR, Hennessey PA, Formica MA, Cox C, Walsh EE (2005) Respiratory Syncytial Virus Infection in Elderly and High-Risk Adults. *New England Journal of Medicine* 352: 1749-1759. doi: doi:10.1056/NEJMoa043951
42. Stewart AJ, Devlin PM (2006) The history of the smallpox vaccine. *Journal of Infection* 52: 329-334.
43. Krugman S (1977) Present status of measles and rubella immunization in the United States: A medical progress report. *The Journal of Pediatrics* 90: 1-12.

44. Weibel RE, Stokes J, Buynak EB, Whitman JE, Hilleman MR (1967) Live, Attenuated Mumps-Virus Vaccine. *New England Journal of Medicine* 276: 245-251. doi: doi:10.1056/NEJM196702022760501
45. Kim HW, Canchola JG, Brandt CD, Pyles G, Chanock RM, Jensen K, Parrott RH (1969) Respiratory Syncytial Virus Disease in Infants Despite Prior Administration of Antigenic Inactivated Vaccine. *American Journal of Epidemiology* 89: 422-434.
46. McLellan JS, Yang Y, Graham BS, Kwong PD (2011) Structure of respiratory syncytial virus fusion glycoprotein in the postfusion conformation reveals preservation of neutralizing epitopes. *Journal of virology* 85: 7788-7796. doi: 10.1128/JVI.00555-11
47. El Omari K, Dhaliwal B, Ren J, Abrescia NGA, Lockyer M, Powell KL, Hawkins AR, Stammers DK (2011) Structures of respiratory syncytial virus nucleocapsid protein from two crystal forms: details of potential packing interactions in the native helical form. *Acta crystallographica Section F, Structural biology and crystallization communications* 67: 1179-1183. doi: 10.1107/S1744309111029228
48. Money Va, McPhee HK, Mosely Ja, Sanderson JM, Yeo RP (2009) Surface features of a Mononegavirales matrix protein indicate sites of membrane interaction. *Proceedings of the National Academy of Sciences of the United States of America* 106: 4441-4446. doi: 10.1073/pnas.0805740106
49. Tawar RG, Duquerroy S, Vonnrhein C, Varela PF, Damier-Piolle L, Castagné N, MacLellan K, Bedouelle H, Bricogne G, Bhella D, Eléouët J-F, Rey Fa (2009) Crystal structure of a nucleocapsid-like nucleoprotein-RNA complex of respiratory syncytial virus. *Science (New York, NY)* 326: 1279-1283. doi: 10.1126/science.1177634
50. Joncas JH, Williams R, Berthiaume L, Beaudry P, Pavilanis V (1969) DIAGNOSIS OF VIRAL RESPIRATORY INFECTIONS BY ELECTRON MICROSCOPY. *The Lancet* 293: 956-959.
51. Jeffree C (2003) Distribution of the attachment (G) glycoprotein and GM1 within the envelope of mature respiratory syncytial virus filaments revealed using field emission scanning electron microscopy. *Virology* 306: 254-267. doi: 10.1016/S0042-6822(02)00016-8
52. Jeffree CE, Brown G, Aitken J, Su-Yin DY, Tan B-H, Sugrue RJ (2007) Ultrastructural analysis of the interaction between F-actin and respiratory syncytial virus during virus assembly. *Virology* 369: 309-323. doi: 10.1016/j.virol.2007.08.007
53. Gower TL, Pastey MK, Peeples ME, Peter L, Mccurdy LH, Hart TK, Guth A, Johnson TR, Graham BS, Collins PL (2005) RhoA Signaling Is Required for Respiratory Syncytial Virus-Induced Syncytium Formation and Filamentous Virion Morphology RhoA Signaling Is Required for Respiratory Syncytial Virus-

- Induced Syncytium Formation and Filamentous Virion Morphology. Society. doi: 10.1128/JVI.79.9.5326
54. Bächli T (1988) Direct observation of the budding and fusion of an enveloped virus by video microscopy of viable cells. *The Journal of cell biology* 107: 1689-1695.
  55. Liljeroos L, Huiskonen JT, Ora A, Susi P, Butcher SJ (2011) Electron cryotomography of measles virus reveals how matrix protein coats the ribonucleocapsid within intact virions. *Proceedings of the National Academy of Sciences of the United States of America* 108: 18085-18090. doi: 10.1073/pnas.1105770108
  56. Loney C, Mottet-Osman G, Roux L, Bhella D (2009) Paramyxovirus ultrastructure and genome packaging: cryo-electron tomography of sendai virus. *Journal of Virology* 83: 8191-8197. doi: JVI.00693-09 [pii]
  57. Huang YT, Collins PL, Wertz GW (1985) Characterization of the 10 proteins of human respiratory syncytial virus: identification of a fourth envelope-associated protein. *Virus research* 2: 157-173.
  58. Fearn R, Collins PL (1999) Role of the M2-1 Transcription Antitermination Protein of Respiratory Syncytial Virus in Sequential Transcription. *Journal of Virology* 73: 5852-5864.
  59. Collins PL, Hill MG, Cristina J, Grosfeld H (1996) Transcription elongation factor of respiratory syncytial virus, a nonsegmented negative-strand RNA virus. *Proceedings of the National Academy of Sciences* 93: 81-85.
  60. Cheng X, Park H, Zhou H, Jin H (2005) Overexpression of the M2-2 Protein of Respiratory Syncytial Virus Inhibits Viral Replication. *Journal of Virology* 79: 13943-13952. doi: 10.1128/jvi.79.22.13943-13952.2005
  61. Flint SJ, American Society for Microbiology. (2009) *Principles of virology*. ASM Press, Washington, DC
  62. Kallewaard NL, Bowen AL, Crowe Jr JE (2005) Cooperativity of actin and microtubule elements during replication of respiratory syncytial virus. *Virology* 331: 73-81.
  63. Bukreyev A, Whitehead SS, Murphy BR, Collins PL (1997) Recombinant respiratory syncytial virus from which the entire SH gene has been deleted grows efficiently in cell culture and exhibits site-specific attenuation in the respiratory tract of the mouse. *Journal of Virology* 71: 8973-8982.
  64. Harrison MS, Sakaguchi T, Schmitt AP (2010) Paramyxovirus assembly and budding: building particles that transmit infections. *The international journal of biochemistry & cell biology* 42: 1416-1429. doi: 10.1016/j.biocel.2010.04.005
  65. Lazzarini RA, Keene JD, Schubert M (1981) The origins of defective interfering particles of the negative-strand RNA viruses. *Cell* 26: 145-154.

66. Teng MN, Collins PL (1998) Identification of the respiratory syncytial virus proteins required for formation and passage of helper-dependent infectious particles. *Journal of virology* 72: 5707-5716.
67. Ghildyal R, Mills J, Murray M, Vardaxis N, Meanger J (2002) Respiratory syncytial virus matrix protein associates with nucleocapsids in infected cells. *The Journal of general virology* 83: 753-757.
68. Li D, Jans DA, Bardin PG, Meanger J, Mills J, Ghildyal R (2008) Association of respiratory syncytial virus M protein with viral nucleocapsids is mediated by the M2-1 protein. *J Virol* 82: 8863-8870. doi: JVI.00343-08 [pii]
69. Coronel EC, Murti KG, Takimoto T, Portner A (1999) Human parainfluenza virus type 1 matrix and nucleoprotein genes transiently expressed in mammalian cells induce the release of virus-like particles containing nucleocapsid-like structures. *J Virol* 73: 7035-7038.
70. Takimoto T, Murti KG, Bousse T, Scroggs RA, Portner A (2001) Role of matrix and fusion proteins in budding of Sendai virus. *J Virol* 75: 11384-11391. doi: 10.1128/JVI.75.23.11384-11391.2001
71. Ciancanelli MJ, Basler CF (2006) Mutation of YMYL in the Nipah virus matrix protein abrogates budding and alters subcellular localization. *J Virol* 80: 12070-12078. doi: JVI.01743-06 [pii]
72. Li M, Schmitt PT, Li Z, McCrory TS, He B, Schmitt AP (2009) Mumps virus matrix, fusion, and nucleocapsid proteins cooperate for efficient production of virus-like particles. *J Virol* 83: 7261-7272. doi: JVI.00421-09 [pii]
73. Schmitt AP, Leser GP, Waning DL, Lamb RA (2002) Requirements for budding of paramyxovirus simian virus 5 virus-like particles. *Journal of virology* 76: 3952-3964.
74. Henderson G, Murray J, Yeo RP (2002) Sorting of the respiratory syncytial virus matrix protein into detergent-resistant structures is dependent on cell-surface expression of the glycoproteins. *Virology* 300: 244-254.
75. Giuffre RM, Tovell DR, Kay CM, Tyrrell DL (1982) Evidence for an interaction between the membrane protein of a paramyxovirus and actin. *Journal of Virology* 42: 963-968.
76. Tyrrell DL, Norrby E (1978) Structural polypeptides of measles virus. *The Journal of general virology* 39: 219-229.
77. Fernie BF, Gerin JL (1982) Immunochemical identification of viral and nonviral proteins of the respiratory syncytial virus virion . *Immunochemical Identification of Viral and Nonviral Proteins of the Respiratory Syncytial Virus Virion* 37.
78. Gupta S, De BP, Drazba JA, Banerjee AK (1998) Involvement of Actin Microfilaments in the Replication of Human Parainfluenza Virus Type 3. *Journal of Virology* 72: 2655-2662.

79. Moyer SA, Baker SC, Lessard JL (1986) Tubulin: a factor necessary for the synthesis of both Sendai virus and vesicular stomatitis virus RNAs. *Proceedings of the National Academy of Sciences* 83: 5405-5409.
80. Moyer SA, Baker SC, Horikami SM (1990) Host cell proteins required for measles virus reproduction. *Journal of General Virology* 71: 775-783. doi: 10.1099/0022-1317-71-4-775
81. Burke E, Dupuy L, Wall C, Barik S (1998) Role of cellular actin in the gene expression and morphogenesis of human respiratory syncytial virus. *Virology* 252: 137-148. doi: 10.1006/viro.1998.9471
82. Burke E, Mahoney NM, Almo SC, Barik S (2000) Profilin Is Required for Optimal Actin-Dependent Transcription of Respiratory Syncytial Virus Genome RNA. *Journal of virology* 74: 669-675. doi: 10.1128/JVI.74.2.669-675.2000
83. Narumiya S (1996) The small GTPase Rho: cellular functions and signal transduction. *J Biochem* 120: 215-228.
84. Pastey MK, Crowe JE, Jr., Graham BS (1999) RhoA interacts with the fusion glycoprotein of respiratory syncytial virus and facilitates virus-induced syncytium formation. *J Virol* 73: 7262-7270.
85. Yao Q, Compans RW (2000) Filamentous particle formation by human parainfluenza virus type 2. *J Gen Virol* 81: 1305-1312.
86. Schowalter RM, Wurth MA, Aguilar HC, Lee B, Moncman CL, McCann RO, Dutch RE (2006) Rho GTPase activity modulates paramyxovirus fusion protein-mediated cell-cell fusion. *Virology* 350: 323-334. doi: S0042-6822(06)00062-6
87. Pastey MK, Gower TL, Spearman PW, Crowe JE, Jr., Graham BS (2000) A RhoA-derived peptide inhibits syncytium formation induced by respiratory syncytial virus and parainfluenza virus type 3. *Nat Med* 6: 35-40. doi: 10.1038/71503
88. Wurth MA, Schowalter RM, Smith EC, Moncman CL, Dutch RE, McCann RO (2010) The actin cytoskeleton inhibits pore expansion during PIV5 fusion protein-promoted cell-cell fusion. *Virology* 404: 117-126.
89. Utley TJ, Ducharme Na, Varthakavi V, Shepherd BE, Santangelo PJ, Lindquist ME, Goldenring JR, Crowe JE (2008) Respiratory syncytial virus uses a Vps4-independent budding mechanism controlled by Rab11-FIP2. *Proceedings of the National Academy of Sciences of the United States of America* 105: 10209-10214. doi: 10.1073/pnas.0712144105
90. Santangelo PJ, Lifland AW, Curt P, Sasaki Y, Bassell GJ, Lindquist ME, Jr JEC, America N (2009) Single molecule – sensitive probes for imaging RNA in live cells. *Nature Methods* 6: 10-14. doi: 10.1038/NMETH.1316
91. Bharat TAM, Riches JD, Kolesnikova L, Welsch S, Krähling V, Davey N, Parsy M-L, Becker S, Briggs JAG (2011) Cryo-Electron Tomography of Marburg Virus

- Particles and Their Morphogenesis within Infected Cells. *PLoS biology* 9: e1001196. doi: 10.1371/journal.pbio.1001196
92. Beniac DR, Melito PL, Devarenes SL, Hiebert SL, Rabb MJ, Lamboo LL, Jones SM, Booth TF (2012) The organisation of Ebola virus reveals a capacity for extensive, modular polyploidy. *PloS one* 7: e29608. doi: 10.1371/journal.pone.0029608
  93. Bächli T, Howe C (1973) Morphogenesis and ultrastructure of respiratory syncytial virus. *Journal of virology* 12: 1173-1180.
  94. Guichard P, Krell T, Chevalier M, Vaysse C, Adam O, Ronzon F, Marco S (2011) Three dimensional morphology of rabies virus studied by cryo-electron tomography. *Journal of structural biology*. doi: 10.1016/j.jsb.2011.07.003
  95. Harris A, Cardone G, Winkler DC, Heymann JB, Brecher M, White JM, Steven AC (2006) Influenza virus pleiomorphy characterized by cryoelectron tomography. *Proceedings of the National Academy of Sciences of the United States of America* 103: 19123-19127. doi: 10.1073/pnas.0607614103
  96. Strecker T, Eichler R, Meulen J, Weissenhorn W, Dieter Klenk H, Garten W, Lenz O (2003) Lassa virus Z protein is a matrix protein and sufficient for the release of virus-like particles [corrected]. *J Virol* 77: 10700-10705.
  97. Mastronarde DN (2005) Automated electron microscope tomography using robust prediction of specimen movements. *Journal of structural biology* 152: 36-51. doi: 10.1016/j.jsb.2005.07.007
  98. Mason SW, Aberg E, Lawetz C, DeLong R, Whitehead P, Liuzzi M (2003) Interaction between Human Respiratory Syncytial Virus (RSV) M2-1 and P Proteins Is Required for Reconstitution of M2-1-Dependent RSV Minigenome Activity. *Journal of virology* 77: 10670-10676. doi: 10.1128/JVI.77.19.10670-10676.2003
  99. Rigort A, Gunther D, Hegerl R, Baum D, Weber B, Prohaska S, Medalia O, Baumeister W, Hege HC (2011) Automated segmentation of electron tomograms for a quantitative description of actin filament networks. *J Struct Biol* 177: 135-144. doi: S1047-8477(11)00251-6
  100. Jen TC, Hsieh B, Wang SJ (2005) Image contrast enhancement based on intensity-pair distribution. *Proceedings of IEEE International Conference on Image Processing ICIP, Genova, Italy*, pp. 913-916.
  101. Kabir H, M. A-A-W, O C (2009) Global and Local Transformation Function Mixture for Image Contrast Enhancement. *Digest of Technical Papers International Conference on Consumer Electronics, Las Vegas, NV*, pp. 1-2.